Parametric Experimentation to Evaluate Chiral Bars Representative of Granular Motif

Nima Nejadsadeghi, François Hild, Anil Misra

Parametric Experimentation to Evaluate Chiral Bars Representative of Granular Motif

Nima Nejadsadeghi[1], Francois Hild[2], and Anil Misra[3*]

[1]Mechanical Engineering Department,
University of Kansas, 1530 W 15th Street, Learned Hall, Lawrence, KS 66047-7609, USA
[2]Université Paris-Saclay, CentraleSupélec, ENS Paris-Saclay, CNRS
LMPS - Laboratoire de Mécanique Paris-Saclay, 91190 Gif-sur-Yvette, France
[3]Civil, Environmental and Architectural Engineering Department,
University of Kansas, 1530 W 15th Street, Learned Hall, Lawrence, KS 66045-7609, USA.
*corresponding author: Ph: (785) 864-1750, Fax: (785) 864-5631, Email: amisra@ku.edu

Abstract

The recent wide-ranging interest in chiral materials motivates the need to understand the mechanisms that underlie mechanical chirality. This paper investigates the emergent chiral mechanical behavior of bars in relationship to microscale deformation mechanisms. The focus is upon (meta)material systems with granular motif that exploit couplings between stretch, shear and rotation such that the designed bar exhibits non-standard transverse motion under extension. To this end, a 1D-micropolar model is derived using the granular micromechanics paradigm to predict macroscale chirality based upon grain-scale interactions. The model provides micro-macro links necessary for designing the physical (meta)material system conceived as a granular bar. The validity of the derived model is then investigated through parametric experimentation using the designed system fabricated through 3D printing. The granular bar is varied with regard to two geometrical parameters that describe the interaction between two adjacent grains, thereby providing parametric spaces with respect to the considered geometrical parameters. Tensile experiments on the granular bar are analyzed using digital image correlation (DIC) to extract multiscalar deformation fields. The DIC results serve as the basis for investigating the unusual motions predicted by the 1D model by comparing the predicted displacement and rotation fields with those obtained experimentally.

Keywords: Granular material; Microstructures; Mechanical tests; Energy methods; Chirality.

1. INTRODUCTION

A material system is deemed to exhibit a chiral behavior when the properties of plane-mirrored images cannot be mapped onto themselves by coordinate transformations consisting of rotations and translations alone following the concept discussed by Kelvin [1]. The significance of chirality lies in its applications in diverse branches of science, including physics, biology, and optics [2–5]. In the emerging field of metamaterials, vibration attenuation and negative coefficient of thermal expansion materials are applications that are being developed to exploit material chirality (see the review paper [6] for a more exhaustive list of applications of chiral metamaterials).

Along these lines, chiral lattices have been extensively studied in terms of their phononic properties [7–10]. For example, the effect of geometrical parameters of such lattices on their band structure has been investigated [7]. The wave propagation characteristics of hexagonal chiral lattices have also been modeled as second gradient media [8]. Further, the effect of chirality on rotation of the polarization axis has been recently investigated experimentally in mechanical metamaterials [11]. The concept of chirality in lattices has also been extended to chiral metacomposites by including inclusions in order to obtain low-frequency stop bands in their band structure [9].

It is remarkable that chiral effects are also present in static mechanical systems. Several recent works have attempted to address the static deformation characteristics of chiral media. For instance, the elastic constants were related to in-plane deformation of different chiral honeycombs through finite element modeling and experiment [12]. Moreover, a homogenization scheme was implemented in a finite element setting to obtain effective mechanical properties over a unit-cell [13]. However, classical Cauchy elasticity was not sufficient to fully predict chirality as was experimentally shown by analyzing the deformation of a 2D non-centro-symmetric lattice under static load [14]. In recent years, generalized continuum mechanics theories (such as micropolar, micromorphic and Willis elasticity) have been adopted to address the shortcomings of classical continuum mechanics in describing chirality [10,15–27].

The literature on lattice chirality offers comprehensive studies on properties of particular pre-designed microstructural units using novel experimental and numerical schemes (see for example [25,27–30]). However, to obtain a deeper understanding of emergent macroscale mechanical chirality, a general analysis is needed to determine the effect of different contributing microscale factors. The focus is hereafter put upon (meta)material systems with granular motif that can be described as composed of nearly rigid elements (or grains) in which the elastic strain energy is stored in deformable interconnections or interfaces between the grains [31]. Such systems are representative of many materials with granular microstructures in which the deformation of an interacting grain-pair can be effectively described in terms of the relative motions of

the grain centroids/barycenters regardless of the location of the actual deformation within the grains [31,32]. The chirality in this material system is introduced by exploiting the coupling between grain-pair relative stretch and rotation by designing appropriate grain-pair interaction mechanisms. With the view of keeping the analysis tractable, the simplest conceivable 1D mathematical model of chiral media is considered by including particular mechanisms that lead to a macroscale behavior distinguished by a specific axis/plane of chirality. In this context, let us note that in "classic" chiral beams, the chirality often relates to the axis of the beam under consideration. The typical example of such "classic" chiral beams is naturally twisted rods coupling torsion and stretch, such as those in biological molecules, in liquid crystals of cholesteric type, and in wire ropes [33–36]. Chirality of the mechanical behavior is known to manifest itself differently in systems that may be treated using 3D, 2D or 1D models. In the present work, the designed grain-pair interaction mechanisms considering stretch-rotation coupling leads to a 1D system with properties such that the axis of chirality is orthogonal to the beam axis.

In the present paper, granular micromechanics approach (GMA) [32] is applied to derive a novel 1D-micropolar model of a chiral bar that includes couplings between different deformation-modes of a bar, including stretch, bending and shear. It is shown that the derived model, with the included couplings, predicts non-standard transverse deformations and rotations as well as a chiral behavior in bars subjected to uniaxial loadings. These predictions are compared to experiments performed on bars fabricated by closely mimicking the modeling approach. A 1D model was derived with the intent of keeping the theoretical analysis and its experimental evaluation, including the fabrication of physical systems (metamaterial), as simple as possible. It is noteworthy that, to the authors' best knowledge, no other such models, theoretical predictions, experimental results and their evaluations exist in the literature.

In the following discussion, the granular micromechanics approach (GMA) of micro-macro links [31,32] is first utilized to develop a micropolar model with the lowest dimension capable of exhibiting chirality in a 1D granular bar placed in a 2D deformation plane. The motivation is to develop a tractable model that provides micro-macro links and opens an avenue for rigorous analyses of the role of different non-standard deformation mechanisms (i.e., transverse deformation and rotation) on chirality of a bar under axial loading. An example of a chiral granular bar is then proposed with a particular grain-pair interaction and fabricated using 3D printing. The proposed granular bar is then studied under uniaxial loading through parametric experimentation by altering the geometrical parameters that govern the grain-pair interaction mechanisms. The deformation mechanisms of the bar are analyzed by using Digital image correlation (DIC) to obtain full-field deformation measurements from the investigated experiments. Last, the model parameters are calibrated to the experimental results, where the effect of the alteration in grain-pair interactions on the deformation behavior and the range of validity of the micropolar model are discussed.

2. MATERIALS AND METHODS

This section is categorized into two main parts. The first part (subsection 2.1) gives the derivation of the 1D micropolar model following GMA. The derivation proceeds by establishing the identification of grain motions with continuum displacement. Constitutive equations are introduced, the principle of virtual work is applied to determine the governing equations, and their non-dimensional form is then obtained. Further, analytical solutions are obtained for uniaxial extensions. The second part (subsection 2.2) describes the parametric experimentation for verifying the derived model. The design and fabrication of granular bars is described, the experimental procedure and image acquisition protocol is given, and the procedure for digital image correlation is introduced.

2.1. Micropolar Chiral Model using GMA

For a micromorphic model of degree 1 of a 3D material with granular microstructure, the displacement of grains within a volume element, adopting the summation convention over repeated indices, is described as [32,37]

$$\phi_i = \bar{\phi}_i + \psi_{ij} x'_j + \psi_{ijk} x'_j x'_k , \tag{1}$$

where $\bar{\phi}_i$ is the displacement of the center of mass of the volume element in the macroscale coordinate system x_i, ψ_{ij} and ψ_{ijk} second and third rank micro-deformation tensors, respectively. In Eq. (1), $\bar{\phi}_i$, ψ_{ij}, and ψ_{ijk} are all functions of x_i only, and x'_i is the microscale coordinate system parallel to the macroscale coordinate system x_i, and attached to the center of mass of the volume element. Note that Eq. (1) assumes continuity in both macro- and microscales [32] in the sense of Piola's Ansatz for micro-macro kinematic identification (see for example [26,31,38]) and considers infinitesimal deformations of the granular solid.

The kinematic description in Eq. (1) encodes sufficient microscale information to model both randomly-packed granular materials and (tailored) metamaterials with granular mesostructures. Certain assumptions on the nature of the microdeformation tensors ψ_{ij} and ψ_{ijk} have been shown to result in micropolar and second gradient theories [32]. In the present paper, the kinematic description of Eq. (1) is particularized to describe a 1D granular-mesostructured solid (termed here as granular bar) in the 2D $x_1 x_2$ deformation plane. In that case, the displacement only depends on x_1 and x'_1. As a result, Eq. (1) is written in component form as

$$\phi_1 = \bar{\phi}_1 + \psi_{11} x_1' + \psi_{111} x_1' x_1', \qquad \phi_2 = \bar{\phi}_2 + \psi_{21} x_1' + \psi_{211} x_1' x_1'. \tag{2}$$

For further discussion, the following micro-macro relative measures are introduced [26,32]

$$\gamma_{11} = \bar{\phi}_{1,1} - \psi_{11}, \quad \gamma_{111} = \psi_{11,1} - \psi_{111}, \quad \gamma_{21} = \bar{\phi}_{2,1} - \psi_{21}, \quad \gamma_{211} = \psi_{21,1} - \psi_{211}, \tag{3}$$

where differentiation with respect to spatial coordinates x_1 is denoted by a comma in the subscript. If only ϕ_1 is considered with $\gamma_{111} = 0$, the corresponding model is termed as micromorphic rod model of degree 1 [32]. This form accounts for micro-macro transfer of energy (coupling) and length scale effects in the axial deformation of rods. If it is further assumed that $\gamma_{11} = 0$, the result is a second gradient model of a rod incorporating length scale effects [39]. Within the scope of the present paper, the case considered is the one in which the kinematic measure ψ_{111} vanishes (such that the polynomial expansion of ϕ_1 is up to linear terms in x_1'.), and the micro-macro relative measure $\gamma_{11} = 0$, which leads to $\psi_{11} = \bar{\phi}_{1,1}$. This consideration yields the simplest (classical model) model in the x_1 direction that is needed for modeling chirality in a micropolar medium [19,26]. For the kinematic description of the system in the x_2 direction (ϕ_2), the following condition is assumed $\gamma_{211} = 0 \rightarrow \psi_{211} = \psi_{21,1}$. As a result, there remains only one independent microscale kinematic measure, ψ_{21}. Considering Eq. (3) and the afore-mentioned simplifications, Eq. (2) reduces to

$$\phi_1 = \bar{\phi}_1 + \bar{\phi}_{1,1} x_1', \qquad \phi_2 = \bar{\phi}_2 + \psi_{21} x_1' + \psi_{21,1} x_1' x_1'. \tag{4}$$

It is worth noting that the considered kinematic description given in Eq. (4) can be further simplified to other recognized models. For instance, neglecting any macroscale motion in the x_1 direction results in the classical Timoshenko beam kinematics, while further constraining the system to have $\gamma_{21} = 0 \rightarrow \psi_{21} = \bar{\phi}_{2,1}$ yields the Euler-Bernoulli kinematics.

The objective relative displacement of two neighboring grains *n* and *p* using Eq. (4) becomes

$$\begin{aligned} \delta_1^{np} &= \phi_1^p - \phi_1^n = \bar{\phi}_{1,1} J_1^{np}, \\ \delta_2^{np} &= \phi_2^p - \phi_2^n = \psi_{21} J_1^{np} + \psi_{21,1} J_2^{np} = \bar{\phi}_{2,1} J_1^{np} - \gamma_{21} J_1^{np} + \psi_{21,1} J_2^{np}, \end{aligned} \tag{5}$$

where $J_1^{np} = l_1^p - l_1^n$ and $J_2^{np} = l_1^p l_1^p - l_1^n l_1^n$ are geometry moment measures, and l_1^q the vector joining the center of mass of the volume element to grain *q* centroid in the x_1 direction. In Eq. (5), three different microscale (grain-pair) kinematic measures are recognized

$$\delta_{\mathrm{n}} = \bar{\phi}_{1,1} J_1^{np}, \quad \delta_{\mathrm{s}} = \gamma_{21} J_1^{np}, \quad \delta_{\theta} = \psi_{21,1} J_2^{np}, \tag{6}$$

where δ_{n} is the classical continuum relative displacement in the x_1 direction, δ_{s} the relative displacement in the x_2 direction due to the fluctuations between the macroscale displacement gradient $\bar{\phi}_{2,1}$ and the microscale kinematic measure ψ_{21}, and δ_{θ} a portion of relative displacement in the x_2 direction due to the second gradient effect (also interpretable as the gradient of rotation field).

2.1.1. Constitutive equations

Let us consider the macroscale deformation energy density *W* to be a function of the continuum kinematic measures, namely, $W = W(\bar{\phi}_{1,1}, \gamma_{21}, \psi_{21,1})$. It is worth noting that the macroscale deformation energy density *W* needs to be invariant with respect to rigid body motions, and hence, the term $\bar{\phi}_{2,1}$ alone cannot be a part of its description.

Conjugates to the continuum kinematic measures, namely, macroscale stress measures, are introduced as

$$\tau_{11} = \frac{\partial W}{\partial \bar{\phi}_{1,1}}, \quad \sigma_{21} = \frac{\partial W}{\partial \gamma_{21}}, \quad \mu_{211} = \frac{\partial W}{\partial \psi_{21,1}}, \tag{7}$$

where τ_{11} is recognized as the Cauchy stress, σ_{21} as the relative stress, and μ_{211} as the double stress. The macroscale deformation energy density, *W,* is also obtained as the accumulation of the microscale grain-pair deformation energy expressed in terms of the microscale kinematic measures [31-32, 40]

$$W = \frac{1}{L'} \sum_{\alpha} W^{\alpha} \left(\delta_{\mathrm{n}}, \delta_{\mathrm{s}}, \delta_{\theta} \right), \tag{8}$$

where W^{α} is the microscale deformation energy calculated per unit bar cross-sectional area for the α^{th} interacting grain pair in the bar volume element (VE) of size *L'*. Conjugates to the microscale kinematic measures, namely, grain-pair forces (and moments) f_{n}, f_{s}, and f_{θ}, also calculated per unit bar cross-sectional area are defined as

$$f_{\mathrm{n}} = \frac{\partial W^{\alpha}}{\partial \delta_{\mathrm{n}}}, \quad f_{\mathrm{s}} = \frac{\partial W^{\alpha}}{\partial \delta_{\mathrm{s}}}, \quad f_{\theta} = \frac{\partial W^{\alpha}}{\partial \delta_{\theta}}. \tag{9}$$

Substituting Eq. (8) into Eq. (7) and employing Eqs. (6) and (9), the macroscale stress measures are linked to the corresponding force measures through

$$\tau_{11} = \frac{1}{L'} \sum_{\alpha} f_{\mathrm{n}}{}^{\alpha} J_1^{\alpha}, \quad \sigma_{21} = \frac{1}{L'} \sum_{\alpha} f_{\mathrm{s}}{}^{\alpha} J_1^{\alpha}, \quad \mu_{211} = \frac{1}{L'} \sum_{\alpha} f_{\theta}{}^{\alpha} J_2^{\alpha}. \tag{10}$$

In Eq. (10) it is noted that J_1^{α} and J_2^{α} for the α^{th} grain-pair for interacting grains *n* and *p* are evaluated as J_1^{np} and J_2^{np}, respectively.

To obtain constitutive equations at both micro- and macroscales, an expression for the microscale deformation energy W^{α} is postulated. As a first approximation toward linking the micro-mechano-morphology of a granular-mesostructured medium to its emergent macroscopic chiral behavior, only linear elastic mechanisms of deformation are considered. Therefore, the following quadratic expression for the microscale deformation energy W^{α} for the α^{th} grain pair is considered

$$W^{\alpha} = \frac{1}{2} K_{\mathrm{n}}{}^{\alpha} \left(\delta_{\mathrm{n}}^{\alpha}\right)^2 + \frac{1}{2} K_{\mathrm{s}}{}^{\alpha} \left(\delta_{\mathrm{s}}^{\alpha}\right)^2 + \frac{1}{2} K_{\theta}{}^{\alpha} \left(\delta_{\theta}^{\alpha}\right)^2 + K_{\mathrm{ns}}{}^{\alpha} \delta_{\mathrm{n}}^{\alpha} \delta_{\mathrm{s}}^{\alpha} + K_{\mathrm{n}\theta}{}^{\alpha} \delta_{\mathrm{n}}^{\alpha} \delta_{\theta}^{\alpha} + K_{\mathrm{s}\theta}{}^{\alpha} \delta_{\mathrm{s}}^{\alpha} \delta_{\theta}^{\alpha}. \tag{11}$$

In Eq. (11), K_i^{α}, where $i \in \{\mathrm{n}, \mathrm{s}, \theta, \mathrm{ns}, \mathrm{n}\theta, \mathrm{s}\theta\}$, are the stiffnesses associated with their corresponding mechanisms for the α^{th} grain pair, all having the dimension of force per length. In particular, $K_{\mathrm{n}}{}^{\alpha}$ is the axial (normal) stiffness, $K_{\mathrm{s}}{}^{\alpha}$ the shear stiffness, and $K_{\theta}{}^{\alpha}$ the rotational stiffness of a grain-pair (see for comparison [40]). The term $K_{\mathrm{ns}}{}^{\alpha}$ couples normal and shear deformations, while $K_{\mathrm{n}\theta}{}^{\alpha}$ and $K_{\mathrm{s}\theta}{}^{\alpha}$ couple normal and rotational, and shear and rotational deformations, respectively, and are included for the sake of completeness inspired by experimental and discrete simulation observations [19], and appear in similar discrete systems [41]. The grain-pair forces introduced in Eq. (9) are obtained using Eq. (11)

$$\begin{aligned} f_{\mathrm{n}} &= K_{\mathrm{n}}{}^{\alpha} \delta_{\mathrm{n}}^{\alpha} + K_{\mathrm{ns}}{}^{\alpha} \delta_{\mathrm{s}}^{\alpha} + K_{\mathrm{n}\theta}{}^{\alpha} \delta_{\theta}^{\alpha}, \\ f_{\mathrm{s}} &= K_{\mathrm{s}}{}^{\alpha} \delta_{\mathrm{s}}^{\alpha} + K_{\mathrm{ns}}{}^{\alpha} \delta_{\mathrm{n}}^{\alpha} + K_{\mathrm{s}\theta}{}^{\alpha} \delta_{\theta}^{\alpha}, \\ f_{\theta} &= K_{\theta}{}^{\alpha} \delta_{\theta}^{\alpha} + K_{\mathrm{n}\theta}{}^{\alpha} \delta_{\mathrm{n}}^{\alpha} + K_{\mathrm{s}\theta}{}^{\alpha} \delta_{\mathrm{s}}^{\alpha}. \end{aligned} \tag{12}$$

Using Eq. (12), the emergent macroscale constitutive relationships (10) are written as

$$\tau_{11} = C^{\mathrm{n}}\bar{\phi}_{1,1} + C^{\mathrm{ns}}\gamma_{21} + C^{\mathrm{n}\theta}\psi_{21,1},$$
$$\sigma_{21} = C^{\mathrm{s}}\gamma_{21} + C^{\mathrm{ns}}\bar{\phi}_{1,1} + C^{\mathrm{s}\theta}\psi_{21,1}, \tag{13}$$
$$\mu_{211} = C^{\theta}\psi_{21,1} + C^{\mathrm{n}\theta}\bar{\phi}_{1,1} + C^{\mathrm{s}\theta}\gamma_{21},$$

where the macroscale stiffnesses $C^{\mathrm{n}}, C^{\mathrm{s}}, C^{\mathrm{ns}}, C^{\mathrm{n}\theta}$, and $C^{\mathrm{s}\theta}$ are defined as

$$C^{\mathrm{n}} = \frac{1}{L'}\sum_{\alpha} K_{\mathrm{n}}{}^{\alpha} J_1^{\alpha} J_1^{\alpha}, \quad C^{\mathrm{s}} = \frac{1}{L'}\sum_{\alpha} K_{\mathrm{s}}{}^{\alpha} J_1^{\alpha} J_1^{\alpha}, \quad C^{\theta} = \frac{1}{L'}\sum_{\alpha} K_{\theta}{}^{\alpha} J_2^{\alpha} J_2^{\alpha},$$
$$C^{\mathrm{ns}} = \frac{1}{L'}\sum_{\alpha} K_{\mathrm{ns}}{}^{\alpha} J_1^{\alpha} J_1^{\alpha}, \quad C^{\mathrm{n}\theta} = \frac{1}{L'}\sum_{\alpha} K_{\mathrm{n}\theta}{}^{\alpha} J_1^{\alpha} J_2^{\alpha}, \quad C^{\mathrm{s}\theta} = \frac{1}{L'}\sum_{\alpha} K_{\mathrm{s}\theta}{}^{\alpha} J_1^{\alpha} J_2^{\alpha}. \tag{14}$$

In general, appropriate scalings of the grain-scale stiffnesses with the VE size *L'* lead to non-trivial macroscale stiffnesses. For the purposes of this work, with the aim of investigating their consequences, it is assumed that all the macroscale stiffnesses exist and are not trivially vanishing. A formal homogenization scheme may be pursued along this line in the future to determine applicable scaling laws. The corresponding macroscale deformation energy density, following Eq. (11) and using Eqs. (7) and (13), becomes

$$W = \frac{1}{2}C^{\mathrm{n}}\left(\bar{\phi}_{1,1}\right)^2 + \frac{1}{2}C^{\mathrm{s}}\left(\gamma_{21}\right)^2 + \frac{1}{2}C^{\theta}\left(\psi_{21,1}\right)^2 + C^{\mathrm{ns}}\bar{\phi}_{1,1}\gamma_{21} + C^{\mathrm{n}\theta}\bar{\phi}_{1,1}\psi_{21,1} + C^{\mathrm{s}\theta}\gamma_{21}\psi_{21,1}, \tag{15}$$

with positive definiteness of energy requiring that

$$C^{\mathrm{n}} > 0, \quad C^{\mathrm{n}}C^{\mathrm{s}} > \left(C^{\mathrm{ns}}\right)^2, \quad C^{\mathrm{n}}C^{\mathrm{s}}C^{\theta} + 2C^{\mathrm{ns}}C^{\mathrm{n}\theta}C^{\mathrm{s}\theta} > C^{\mathrm{n}}\left(C^{\mathrm{s}\theta}\right)^2 + C^{\mathrm{s}}\left(C^{\mathrm{n}\theta}\right)^2 + C^{\theta}\left(C^{\mathrm{ns}}\right)^2. \tag{16}$$

Further, it is notable (from Eqs. (14) and (15)) that keeping only the first term in the microscale deformation energy (Eq. (11)) results in a classical rod model. Further, retaining only the third term in Eq. (11) results in the Euler Bernoulli beam model, while only the second and third terms (in Eq. (11)) yield the Timoshenko beam model, and finally, retaining the first four terms of Eq. (11) leads to a model equivalent to a non-standard Timoshenko beam model [42].

2.1.2 Governing equations

The principle of virtual work, neglecting inertia terms, states that

$$-\delta\breve{W} + \delta\breve{W}_{ext} = 0, \tag{17}$$

where δ is the variation symbol, and the terms $\delta\breve{W}$, and $\delta\breve{W}_{ext}$ are defined in the sequel. In Eq. (17), $\delta\breve{W} = \int_L \delta W dx$ represents the variation of total macroscale deformation energy

$$\delta\breve{W} = -\int_L \tau_{11,1}\delta\bar{\phi}_1 dx - \int_L \sigma_{21,1}\delta\bar{\phi}_2 dx - \int_L \left(\mu_{211,1} + \sigma_{21}\right)\delta\psi_{21} dx + \tau_{11}\delta\bar{\phi}_1\Big|_{x=0}^{x=L} + \sigma_{21}\delta\bar{\phi}_2\Big|_{x=0}^{x=L} + \mu_{211}\delta\psi_{21}\Big|_{x=0}^{x=L} \tag{18}$$

The term $\delta\breve{W}_{ext}$ corresponds to the variation of total external energy. Considering non-contact volumic terms, it is defined as

$$\delta\breve{W}_{ext} = t_1\delta\bar{\phi}_1\Big|_{x=0}^{x=L} + t_2\delta\bar{\phi}_2\Big|_{x=0}^{x=L} + T_{21}\delta\psi_{21}\Big|_{x=0}^{x=L}. \tag{19}$$

In Eq. (19), t_1 and t_2 are the contact tractions in the x_1 and x_2 directions, respectively, and T_{21} the contact double traction. Substituting Eqs. (18) and (19) in Eq. (17) results in the following balance equations

$$\tau_{11,1} = 0, \quad \sigma_{21,1} = 0, \quad \mu_{211,1} + \sigma_{21} = 0. \tag{20}$$

For the constitutive laws (13), assuming the macroscale stiffnesses to have spatial independence (or material homogeneity at the macroscale), the balance equations (20) are recast as

$$\begin{aligned}
&C^{\mathrm{n}}\bar{\phi}_{1,11} + C^{\mathrm{ns}}\bar{\phi}_{2,11} - C^{\mathrm{ns}}\psi_{21,1} + C^{\mathrm{n\theta}}\psi_{21,11} = 0,\\
&C^{\mathrm{ns}}\bar{\phi}_{1,11} + C^{\mathrm{s}}\bar{\phi}_{2,11} - C^{\mathrm{s}}\psi_{21,1} + C^{\mathrm{s\theta}}\psi_{21,11} = 0,\\
&C^{\mathrm{n\theta}}\bar{\phi}_{1,11} + C^{\mathrm{ns}}\bar{\phi}_{1,1} + C^{\mathrm{s\theta}}\bar{\phi}_{2,11} + C^{\mathrm{s}}\bar{\phi}_{2,1} - C^{\mathrm{s}}\psi_{21} + C^{\theta}\psi_{21,11} = 0.
\end{aligned} \tag{21}$$

Moreover, the boundary conditions are evaluated as

$$\begin{aligned}
&\left(t_1 - C^{\mathrm{n}}\bar{\phi}_{1,1} - C^{\mathrm{ns}}\bar{\phi}_{2,1} + C^{\mathrm{ns}}\psi_{21} - C^{\mathrm{n\theta}}\psi_{21,1}\right)\delta\bar{\phi}_1 = 0, \quad \text{at } x = 0,\, x = L,\\
&\left(t_2 - C^{\mathrm{s}}\bar{\phi}_{2,1} + C^{\mathrm{s}}\psi_{21} - C^{\mathrm{ns}}\bar{\phi}_{1,1} - C^{\mathrm{s\theta}}\psi_{21,1}\right)\delta\bar{\phi}_2 = 0, \quad \text{at } x = 0,\, x = L,\\
&\left(T_{21} - C^{\theta}\psi_{21,1} - C^{\mathrm{n\theta}}\bar{\phi}_{1,1} - C^{\mathrm{s\theta}}\bar{\phi}_{2,1} + C^{\mathrm{s\theta}}\psi_{21}\right)\delta\psi_{21} = 0, \quad \text{at } x = 0,\, x = L.
\end{aligned} \tag{22}$$

It is also instructive to compare the current model against the classical Timoshenko beam model with constant parameters. The latter typically does not consider the axial deformation of the beam, and therefore, the first line in Eq. (21) is irrelevant. Moreover, it does not account for couplings between different deformation modes, hence $C^{\mathrm{ns}} = C^{\mathrm{n\theta}} = C^{\mathrm{s\theta}} = 0$. With these restrictions, Eq. (21) takes the simplified form

$$\bar{\phi}_{2,11} - \psi_{21,1} = 0, \quad \bar{\phi}_{2,1} - \psi_{21} + \frac{C^{\theta}}{C^{\mathrm{s}}}\psi_{21,11} = 0, \tag{23}$$

and the natural boundary conditions (22) reduce to

$$t_2 = C^{\mathrm{s}}\gamma_{21}, \quad T_{21} = C^{\theta}\psi_{21,1}. \tag{24}$$

The ratio $\frac{C^{\theta}}{C^{\mathrm{s}}}$ is equivalent to the term $\frac{EI}{\kappa AG}$ in the formulation of classical Timoshenko beams, where A is the cross sectional area, E the Young's modulus, G the shear modulus, I the second moment of inertia, and κ the Timoshenko shear coefficient. Moreover, ψ_{21} represents the angle of rotation of the normal to the mid-surface of the beam, t_2 the shear force, and T_{21} the bending moment. Last, it may be noted that the derived 1D model (Eqs. (21) and (22)) may not be obtained as a simplification of classical micropolar models such as those discussed in [43,44].

2.1.3. Dimensionless form of governing equations

It is convenient to reduce the number of parameters involved in the problem by nondimensionalizing the governing equations (21). To this end, the following dimensionless variables and parameters are introduced

$$\begin{aligned}
&\tilde{\bar{\phi}}_1 = \frac{\bar{\phi}_1}{L}, \quad \tilde{\bar{\phi}}_2 = \frac{\bar{\phi}_2}{L}, \quad \tilde{\psi}_{21} = \psi_{21}, \quad \tilde{x} = \frac{x}{L}, \\
&\alpha_{\mathrm{s}} = \frac{C^{\mathrm{s}}}{C^{\mathrm{n}}}, \quad \alpha_{\mathrm{ns}} = \frac{C^{\mathrm{ns}}}{C^{\mathrm{n}}}, \quad l_{\mathrm{n}\theta} = \frac{1}{L}\frac{C^{\mathrm{n}\theta}}{C^{\mathrm{n}}}, \quad l_{\mathrm{s}\theta} = \frac{1}{L}\frac{C^{\mathrm{s}\theta}}{C^{\mathrm{n}}} \quad l_{\theta} = \frac{1}{L}\sqrt{\frac{C^{\theta}}{C^{\mathrm{n}}}}
\end{aligned} \tag{25}$$

The parameter α_{s} is the ratio of the shear stiffness to the normal (axial) stiffness, and α_{ns} the ratio of the normal-shear coupling stiffness to the normal stiffness. Moreover, $l_{\mathrm{n}\theta}$, $l_{\mathrm{s}\theta}$, and l_{θ} are dimensionless characteristic lengths related to the effective magnitude of normal-rotation coupling stiffness, shear-rotation coupling, and rotational stiffnesses, respectively. With regard to Eq. (25), the dimensionless form of the governing equations (21) reads

$$\begin{aligned}
&\tilde{\bar{\phi}}_{1,11} + \alpha_{\mathrm{ns}}\tilde{\bar{\phi}}_{2,11} - \alpha_{\mathrm{ns}}\tilde{\psi}_{21,1} + l_{\mathrm{n}\theta}\tilde{\psi}_{21,11} = 0, \\
&\alpha_{\mathrm{ns}}\tilde{\bar{\phi}}_{1,11} + \alpha_{\mathrm{s}}\tilde{\bar{\phi}}_{2,11} - \alpha_{\mathrm{s}}\tilde{\psi}_{21,1} + l_{\mathrm{s}\theta}\tilde{\psi}_{21,11} = 0, \\
&l_{\mathrm{n}\theta}\tilde{\bar{\phi}}_{1,11} + \alpha_{\mathrm{ns}}\tilde{\bar{\phi}}_{1,1} + l_{\mathrm{s}\theta}\tilde{\bar{\phi}}_{2,11} + \alpha_{\mathrm{s}}\tilde{\bar{\phi}}_{2,1} - \alpha_{\mathrm{s}}\tilde{\psi}_{21} + l_{\theta}^2\tilde{\psi}_{21,11} = 0.
\end{aligned} \tag{26}$$

The dimensionless spatial domain of the problem is $0 \le \tilde{x} \le 1$, with dimensionless boundary conditions expressed as

$$\begin{aligned}
&\left(\tilde{t}_1 - \tilde{\bar{\phi}}_{1,1} - \alpha_{\mathrm{ns}}\tilde{\bar{\phi}}_{2,1} + \alpha_{\mathrm{ns}}\tilde{\psi}_{21} - l_{\mathrm{n}\theta}\tilde{\psi}_{21,1}\right)\delta\tilde{\bar{\phi}}_1 = 0, \quad \text{at } \tilde{x} = 0,\ \tilde{x} = 1, \\
&\left(\tilde{t}_2 - \alpha_{\mathrm{s}}\tilde{\bar{\phi}}_{2,1} + \alpha_{\mathrm{s}}\tilde{\psi}_{21} - \alpha_{\mathrm{ns}}\tilde{\bar{\phi}}_{1,1} - l_{\mathrm{s}\theta}\tilde{\psi}_{21,1}\right)\delta\tilde{\bar{\phi}}_2 = 0, \quad \text{at } \tilde{x} = 0,\ \tilde{x} = 1, \\
&\left(\tilde{T}_{21} - l_{\theta}^2\tilde{\psi}_{21,1} - l_{\mathrm{n}\theta}\tilde{\bar{\phi}}_{1,1} - l_{\mathrm{s}\theta}\tilde{\bar{\phi}}_{2,1} + l_{\mathrm{s}\theta}\tilde{\psi}_{21}\right)\delta\tilde{\psi}_{21} = 0, \quad \text{at } \tilde{x} = 0,\ \tilde{x} = 1,
\end{aligned} \tag{27}$$

where $\tilde{t}_1 = \frac{t_1}{C^{\mathrm{n}}}$, $\tilde{t}_2 = \frac{t_2}{C^{\mathrm{n}}}$, and $\tilde{T}_{21} = \frac{T_{21}}{C^{\mathrm{n}} L}$ are dimensionless normal traction (axial force), shear traction (shear force), and contact double traction (bending moment), respectively.

2.1.4. Closed-form solution for tensile testing

Let us focus on the general solution to Eq. (26), which after some straightforward manipulations, becomes

$$\begin{aligned}
&\tilde{\tilde{\phi}}_1 = a_0 + a_1\tilde{x} + a_2\tilde{x}^2, \\
&\tilde{\tilde{\phi}}_2 = b_0 + b_1\tilde{x} + b_2\tilde{x}^2 + b_3\tilde{x}^3, \\
&\tilde{\psi}_{21} = e_0 + e_1\tilde{x} + e_2\tilde{x}^2,
\end{aligned} \tag{28}$$

where $b_i, i \in \{0, 1, 2, 3\}$, $a_i, e_i, i \in \{0, 1, 2\}$ are 10 unknown coefficients to be determined. Substituting the solution (28) into the governing equations (26) results in

$$\begin{aligned}
&a_2 = \frac{\alpha_{\mathrm{ns}} l_{\mathrm{s}\theta} - \alpha_{\mathrm{s}} l_{\mathrm{n}\theta}}{\alpha_{\mathrm{s}} - \alpha_{\mathrm{ns}}^2} e_2, \quad b_2 = \frac{1}{2} e_1 + \frac{\alpha_{\mathrm{ns}} l_{\mathrm{n}\theta} - l_{\mathrm{s}\theta}}{\alpha_{\mathrm{s}} - \alpha_{\mathrm{ns}}^2} e_2, \quad b_3 = \frac{e_2}{3}, \\
&\alpha_{\mathrm{ns}} a_1 + \alpha_{\mathrm{s}} b_1 - \alpha_{\mathrm{s}} e_0 + l_{\mathrm{s}\theta} e_1 + \frac{2\alpha_{\mathrm{s}} l_\theta^2 - 2l_{\mathrm{s}\theta}^2 - 2\alpha_{\mathrm{ns}}^2 l_\theta^2 + 4\alpha_{\mathrm{ns}} l_{\mathrm{n}\theta} l_{\mathrm{s}\theta} - 2l_{\mathrm{n}\theta}^2 \alpha_{\mathrm{s}}}{\alpha_{\mathrm{s}} - \alpha_{\mathrm{ns}}^2} e_2 = 0.
\end{aligned} \tag{29}$$

Equation (29) reduces the number of unknowns from 10 to 6, which are determined from the prescribed boundary conditions. To be consistent with the experimental loading condition (described in Section 2.2), let us focus on uniaxial tension with the following boundary conditions

$$\tilde{\tilde{\phi}}_1(\tilde{x}=0) = 0, \quad \tilde{\tilde{\phi}}_1(\tilde{x}=1) = \bar{\phi}_r, \quad \tilde{\tilde{\phi}}_2(\tilde{x}=0) = \tilde{\tilde{\phi}}_2(\tilde{x}=1) = 0, \quad \tilde{\psi}_{21}(\tilde{x}=0) = \tilde{\psi}_{21}(\tilde{x}=1) = 0. \tag{30}$$

Based on Eq. (30), rotation, transverse displacement, and axial displacement are fixed at one end, while, at the other end, rotation and transverse displacement are fixed and the axial displacement $\bar{\phi}_r$ is prescribed such that from Eq. (28)

$$\begin{aligned}
&a_0 = 0, \quad a_0 + a_1 + a_2 = \bar{\phi}_r, \\
&b_0 = 0, \quad b_0 + b_1 + b_2 + b_3 = 0, \\
&e_0 = 0, \quad e_0 + e_1 + e_2 = 0.
\end{aligned} \tag{31}$$

Equation (31), together with Eq. (29) is solved for the unknown coefficients in Eq. (28), resulting in

$$
\begin{aligned}
a_1 &= \frac{\left(-\alpha_{\mathrm{s}} - 12 l_{\theta}^2\right)\left(\alpha_{\mathrm{s}} - \alpha_{\mathrm{ns}}^2\right) + 6\alpha_{\mathrm{s}}\alpha_{\mathrm{ns}} l_{\mathrm{n}\theta} + 12\alpha_{\mathrm{s}} l_{\mathrm{n}\theta}^2 - 6\alpha_{\mathrm{ns}}^2 l_{\mathrm{s}\theta} - 24\alpha_{\mathrm{ns}} l_{\mathrm{n}\theta} l_{\mathrm{s}\theta} + 12 l_{\mathrm{s}\theta}^2}{\kappa}\bar{\phi}_r, \\
a_2 &= \frac{-6\alpha_{\mathrm{ns}}\left(\alpha_{\mathrm{s}} l_{\mathrm{n}\theta} - \alpha_{\mathrm{ns}} l_{\mathrm{s}\theta}\right)}{\kappa}\bar{\phi}_r = \bar{\phi}_r - a_1, \\
b_1 &= \frac{\alpha_{\mathrm{ns}}\left(\alpha_{\mathrm{s}} - \alpha_{\mathrm{ns}}^2 - 6\alpha_{\mathrm{ns}} l_{\mathrm{n}\theta} + 6 l_{\mathrm{s}\theta}\right)}{\kappa}\bar{\phi}_r, \\
b_2 &= \frac{-\alpha_{\mathrm{ns}}\left(3\alpha_{\mathrm{s}} - 3\alpha_{\mathrm{ns}}^2 - 6\alpha_{\mathrm{ns}} l_{\mathrm{n}\theta} + 6 l_{\mathrm{s}\theta}\right)}{\kappa}\bar{\phi}_r, \\
b_3 &= \frac{2\alpha_{\mathrm{ns}}\left(\alpha_{\mathrm{s}} - \alpha_{\mathrm{ns}}^2\right)}{\kappa}\bar{\phi}_r = -b_1 - b_2, \\
e_1 &= -3b_3, \quad e_2 = 3b_3, \quad a_0 = b_0 = e_0 = 0, \\
&\text{where} \quad \kappa = -\alpha_{\mathrm{s}}^2 + \alpha_{\mathrm{s}}\alpha_{\mathrm{ns}}^2 + 12\alpha_{\mathrm{s}} l_{\mathrm{n}\theta}^2 - 12\alpha_{\mathrm{s}} l_{\theta}^2 + 12\alpha_{\mathrm{ns}}^2 l_{\theta}^2 - 24\alpha_{\mathrm{ns}} l_{\mathrm{n}\theta} l_{\mathrm{s}\theta} + 12 l_{\mathrm{s}\theta}^2.
\end{aligned}
\tag{32}
$$

To illustrate model predictions, three granular bar are considered with stiffness constants $\alpha_{\mathrm{s}} = 0.5$, $\alpha_{\mathrm{ns}} = 0.5$, and $l_{\theta} = 0.1$, with different $l_{\mathrm{n}\theta}$ and $l_{\mathrm{s}\theta}$ values as stated in the caption of Fig. 1. The axial displacement $\tilde{\bar{\phi}}_1$ is in general quadratic with respect to $\tilde{x}$, which reduces to a classical linear dependence when $l_{\mathrm{n}\theta} = l_{\mathrm{s}\theta} = 0$. The transverse displacement $\tilde{\bar{\phi}}_2$ is a cubic function of $\tilde{x}$, and vanishes only for the case of vanishing normal-shear coupling stiffness, α_{ns}. Further, only in the particular case of vanishing characteristic lengths, $l_{\mathrm{n}\theta} = l_{\mathrm{s}\theta} = 0$, the midpoint of the granular bar overlaps with the inflection point of the transverse displacement field. This symmetry-like behavior is broken for non-vanishing $l_{\mathrm{n}\theta}$ or $l_{\mathrm{s}\theta}$, where the inflection point moves to some other location within or outside of the problem domain depending on the values of the characteristic lengths, $l_{\mathrm{n}\theta}$ and $l_{\mathrm{s}\theta}$. The rotation, $\tilde{\psi}_{21}$, within the granular bar follows a quadratic behavior for non-zero normal-shear coupling stiffness, α_{ns}, with its maximum level occurring at the midpoint of the granular bar. The magnitude of rotation is affected by the characteristic lengths, $l_{\mathrm{n}\theta}$ and $l_{\mathrm{s}\theta}$. The transverse displacement $\tilde{\bar{\phi}}_2$ and rotation, $\tilde{\psi}_{21}$, under uniaxial stretch, are not invariant to mirror transformation, and hence represent a chiral behavior of a 1D continuum.

2.2. Parametric Experimentation

The predictions of the proposed micropolar model introduced above, show that chirality in granular media is tied to the deformation mechanisms of interacting grains modelled by inter-granular stiffnesses. To evaluate these predictions, parametric experiments were performed using 3D printed granular bars, whose design was guided by the micro-macro links that form the basis of the GMA considerations described above. The underlying methodology pursued in this work follows the paradigm of designing metamaterials following a rational design approach based upon predictive theories [45].

2.2.1. Prototypical model design and realization

The needed bar should include grain-pair interconnections designed to achieve the interactions that embody the grain-pair deformation energy postulated in Eq. (11). These interactions include grain-pair relative stretch, shear, rotations and couplings among these mechanism. A schematic of the designed granular bar is shown in Fig. 2(a) where the set of solid beams connecting two grains is considered as the mechanical (rheological) analog of grain-pair interactions. This simple mechanism leads to grain-pair interaction that exhibits shear-normal-rotational couplings as proven using FE models in which each grain and grain-pair connection are treated as composed of classical Cauchy continua [19,42].

To investigate the influences of these deformation mechanisms, the geometrical parameters t and b associated with the mechanical analog of grain-pair interactions were varied, thus enabling for an extensive parametric study. This choice is reported in Fig. 2(a) where each sample with its unique set of parameters t and b is shown with a marker within the domain of geometrical parameters. With regard to the considered granular bar, the sample with the largest weight has almost 16% more than those with the least weight.

The CAD software SolidWorks (Dassault Systems SolidWorks Corporation, Waltham, MA, USA) was used to generate the granular bar geometries based on Fig. 2(a). Each granular bar is composed of 11 grains with an out-of-plane thickness of 4 mm (Fig. 2(b)). This value was chosen to induce 2D planar deformations, while preventing warpage in the fabrication process. The granular bar is terminated at both ends with flat extensions designed to facilitate gripping. The designed granular bars were fabricated with a Low Force Stereolithography 3D printer Form 3 (FormLabs, USA), using the so-called "Durable Resin" monomer, with XY resolution and layer thickness of $\approx 50\,\mu m$. The Young's modulus of the cured resin is nominally 1.0 GPa. The printed samples had a maximum of 0.1 mm variation in b and t parameters with respect to their nominal values. For each granular bar geometry, three samples were 3D printed and tested. Measured data from first two sets of samples were used for model verification, and the additional third test was used for assessing measurement repeatability.

2.2.2. Experimental prescription

An ElectroForce 3200 (TA Instruments) testing machine was utilized to conduct tensile tests on the 3D printed metamaterial. The testing machine is equipped with a load cell of capacity ± 450 N, a measurement uncertainty of 0.1%, and resolution of 1 mN; and a displacement transducer with a range of ± 6.5 mm, a measurement uncertainty of 0.1%, and a resolution of 1 µm. Figure 2(b) shows a snapshot of a granular bar being attached to the testing machine with the grips. The boundary conditions prescribed by the grips on the sample were expected to conform to those of Eq. (30), such that a comparison can be made between the theoretical predictions and experimental results. A total extension of 10 mm (axial strain of ca. 0.095) was applied on the granular bar specimens at a rate of 50 µm/s.

To extract grain kinematic data from the experiments, a speckle pattern was applied on the surface of the samples using black and white paint sprays (Fig, 2(b)). Using a DLSR camera, ten images were acquired in the reference configuration for the purpose of uncertainty quantifications, and consecutive images were taken from the samples during the experiment. The image acquisition setup is shown in Fig. 2(c) with the specifications listed in Table 1. To facilitate the distinction between the printed samples and their environment, a red background was adopted, and soft boxes were used to generate diffusive lighting. The captured images were transformed into black and white for performing DIC registrations.

2.2.3. Digital image correlation (DIC)

The captured images of the experiments were post-processed using DIC to measure full-field deformations at different scales of observation. The Correli 3.0 DIC framework was used in which Hencky-elastic regularization was implemented [46]. DIC is based on the registration of image I_0 in the reference configuration and image I_t in the deformed configuration. The registration is based upon the conservation of gray levels between the two images

$$I_0\left(\mathbf{x}\right) \cong I_t\left(\mathbf{x}+\mathbf{u}\left(\mathbf{x}\right)\right), \tag{33}$$

where **x** is the position vector of each pixel within the domain of interest, and **u** the unknown displacement field. The problem is to find a displacement field **u** such that the sum of squared differences between the reference image $I_0\left(\mathbf{x}\right)$ and the corrected deformed image $I_t\left(\mathbf{x}+\mathbf{u}\left(\mathbf{x}\right)\right)$ is minimized. Let us consider a displacement field **u** with the following form

$$\mathbf{u}\left(\mathbf{x},\mathbf{p}\right) = \sum_i \mathbf{N}_i\left(\mathbf{x},\mathbf{p}\right), \tag{34}$$

where the summation convention for subscripts is not exercised, $\mathbf{p}$ the column vector of sought degrees of freedom, and $\mathbf{N}_i(\mathbf{x},\mathbf{p})$ the *i*-th trial displacement field. We note that the expression for **u** in Eq. (34) can be linear or nonlinear with respect to the degrees of freedom, $\mathbf{p}$, depending on the assumed kinematics. The registration minimizes the squared sum of pixel-wise gray level residual ρ over a region of interest (ROI)

$$\eta^2(\mathbf{p}) = \sum_{\text{ROI}} \rho^2(\mathbf{x},\mathbf{p}), \tag{35}$$

where

$$\rho(\mathbf{x},\mathbf{p}) = I_t\left(\mathbf{x}+\mathbf{u}(\mathbf{x},\mathbf{p})\right) - I_0(\mathbf{x}). \tag{36}$$

The minimization scheme is nonlinear and the degrees of freedom vector $\mathbf{p}$ is obtained by iteration using a Gauss-Newton method [47,48]. When finite-element based kinematics are used (particularly for macroscale and microscale analyses described in Section 3.2), the previous cost function was penalized with the equilibrium gap functional [49] written on displacement increments (i.e., corresponding to Hencky elasticity [50]). For mesoscale analyses (Section 3.2), which measured the rigid body motions of each individual grain, no additional regularization was enforced.

3. RESULTS AND DISCUSSION

The results obtained from the experiments described in Subsection 2.2 and their calibration with the model described in Subsection 2.1 are presented here categorized into three parts. The first part (Subsection 3.1) quantifies the uncertainty in displacement measurements obtained via DIC. The second part (Subsection 3.2) describes the multiscalar DIC and the types of data obtained from these analyses. Last, the third part (subsection 3.3) discusses the evaluation of the micropolar model utilizing the results from multiscalar DIC analyses for all the tested specimens. To this end, model parameter identification and the assessment of goodness-of-fit as well as the repeatability of the model evaluation are carried out. The effect of the geometrical parameters on the deformation mechanism is then investigated.

3.1. Uncertainty Quantification

As a first step, all possible combinations of reference images acquired before the beginning of loading were analyzed to quantify the uncertainty levels of displacements extracted from DIC runs. Ten reference images were acquired such that the total number of DIC analyses for uncertainty quantification was 45. The fluctuations caused by the motion of loading machine actuator during image acquisition were corrected by

subtracting the recorded macroscale axial displacement from the DIC measurements. Similarly, the transverse displacements and rotations were corrected by subtracting the mean transverse displacement and mean rotation, since they were not measured in the loading device. Standard deviations were then calculated for each degree of freedom with respect to the 45 DIC analyses. Table 2 reports the uncertainties for the DIC analyses performed at different spatial scales introduced in the following discussions. As seen in Table 2, the uncertainty of displacement measurements through DIC are almost two orders of magnitude lower than the smallest reported displacement.

It may be noted that when compared to previously reported levels for a similar experiment [51], the uncertainty levels are higher. Notably, in the previous study, the uncertainty levels were evaluated in a different way since only one reference image was available and a series of artificial images with the noise level associated with the background was created. Thus, the previous work did not account for all experimental fluctuations. The present levels are expectedly more realistic in terms of noise floor estimates [52].

3.2. Multiscale DIC Analyses of Grain Bar

Altogether, three sets of 14 grain-bar specimens (42 samples) with different t and b combinations were subjected to tensile loading and imaged as described in Sections 2.2.1 and 2.2.2. As an example, Fig. 3(a) shows the initial, final and three intermediate images of a granular bar with t = 1.2 mm and b = 1 mm. All these experiments were analyzed using the described DIC framework at 3 spatial scales, namely the macro, meso and microscales (see [51] for details of the methods).

3.2.1. Macroscale DIC analyses

The first scale, which is referred herein as macroscale DIC, is that in which the granular bar is assumed to be a continuous bar of homogenous cross-section. Macroscale DIC assumes that the granular bar is a small finite volume of a larger body with indistinguishable grains, and as a result, is useful when macroscale continuum models are to be developed. Additionally, in multiscale DIC, this macroscale analysis serves a secondary purpose as well, as its results provide an initialization for the solution for finer scale DIC analyses that, typically, leads to significantly reduced number of iterations and computational demands. Figure 3(b) shows the finite element discretization of the domain for macroscale DIC using 3-noded (T3) elements with a size of 33 px (about 2 mm). It was observed that no significant gain was obtained by using a finer mesh, and the discretization shown in Fig. 3(b) was deemed sufficient to represent many aspects of the system deformation that are apparent at this first scale.

Figures 3(d,f) show, respectively, the transverse and axial displacements for the macroscale analysis considering the full range of applied stretch. The chiral behavior of the granular bar is observed with resemblance to the theoretical predictions of Fig. 1. With regard to Fig. 3(h), an increase in the root mean square (RMS) gray level residuals suggests that the macroscale analysis becomes less accurate as the deformation progresses. The increase in RMS value is essentially attributed to the kinematic assumptions not being accurate enough when the deformations in the grain-pair interaction mechanisms (beams and bars) become large. This issue is amplified by the fact that the macroscale discretization does not differentiate the granular bar from the background, suggesting the need for finer-scale analyses. Therefore, there is a need to identify a domain encompassing the structure (or the microstructure) of interest with the minimum inclusion of background with the intent to extract further details of the deformations.

3.2.2. Microscale DIC analyses

Accordingly, the nominal geometry of the granular bar (i.e., mask) was created, and a registration was performed, using the same algorithm as in standard DIC, to backtrack the mask image of the granular bar in its initial configuration [49,51]. As a result, the structural domain that includes an insignificant amount of background, if any, is obtained (Fig. 3(c)). This structural domain was spatially discretized using T3 elements size of 10 px (about 0.63 mm). The corresponding mesh is shown in Fig. 3(c). Since the DIC analysis is performed using this mesh that is based upon all structural details, it is referred to as microscale analysis. As mentioned before, microscale analyses were initialized using the corresponding macroscale solution. Fig. 3(e,g) show the transverse and axial displacements in the granular bar, respectively, using microscale DIC. A noticeable similarity is observed between the displacement fields obtained from macro- and microscale analyses. However, the RMS gray level residuals for microscale DIC (Fig. 3(i)) suggests a higher faithfulness compared to macroscale DIC as the deformation progresses since the relative increase in RMS level is significantly lower.

The results from macro- and microscale analyses provide interesting evidence of the presence of chirality. While the printed granular bars may be viewed as a chiral lattice structure (similar to chiral lattices proposed in the literature where deformable/rigid nodes are connected via different beam/rod elements), they may also be deemed as granular (meta-)material with a series of rigid grains interacting with each other through some specific grain-pair interaction mechanisms. To check this hypothesis, the strain distribution is examined within the granular bar (note that strain may be taken as proportional to stress distribution for assumed linear elastic constituent material as a first order approximation). Figure 3(j-l) shows, respectively, the normal strain field in the transverse direction, normal strain field in the axial direction, and shear strain field for the full range of applied deformation based upon microscale analyses. The grains experience negligible deformation compared to the interconnections that define the grain-pair interactions. Further,

Fig. 3(m) shows the results for the dimensionless form of the strain energy measure (square root of strain energy normalized by half of the Young's modulus of the constituent material).

3.2.3. Mesoscale DIC analyses

The distributions shown in Fig. 3(m) confirm that the strain energy is localized in the grain-pair interactions, and not in the grains themselves. Therefore, the construct under consideration may truly be treated as a granular system. Consequently, it is useful to focus on the kinematics of individual grains induced by their interaction mechanisms since such a description may lead to reduced-order descriptions of the bar as a granular medium.

To this end, mesoscale DIC analyses with three degrees of freedom for each grain were performed to extract their rigid motions, namely the axial displacement, t_1, the transverse displacement, t_2, and the rotation, θ, of each grain about its center of mass. For the mesoscale analyses, each grain is considered in a separate region of interest, and therefore, DIC initialized solutions from macroscale analyses were performed on each grain independently. For the purpose of illustration, let us consider the granular bar with t = 1.2 mm and b = 1 mm (Fig. 4). Figure 4(a) shows the RMS gray level residuals corresponding to the 11 grains for all the load-steps indicated by the color-scale. Grain 1 corresponds to that attached to the fixed lower grip, and grain 11 to the moving upper grip. Fig. 4(b) displays the axial displacement of each grain. The transverse displacement of grains is reported in Fig. 4(c), and the rotation of grains in Fig. 4(d). A qualitative agreement is noted between the results shown in Fig. 4 and the theoretical predictions (Fig. 1).

3.3. Model Evaluation

A quantitative evaluation of the granular bar behavior based on the proposed micropolar model is possible by comparing the displacement and rotation fields predicted by the model and those of the experiments as determined by the mesoscale DIC analyses. This approach enables the effect of geometric parameters b and t to be evaluated on the behavior of the system, with no need for identifying the stiffnesses associated with each granular bar. Moreover, it serves as a tool to assess the domain of validity of the model predictions in terms of resultant deformation fields. To this end, the grain positions, axial and transverse displacements were nondimensionalized with respect to the initial length of each bar to harmonize the experimental results with the expressions of Eq. (28). A least-squares optimization with equality constraints was utilized to determine the model parameters (described in Appendix A) and to analyze the goodness-of-fit.

3.3.1. Parameter identification and goodness-of-fit

For further discussion, it is advantageous to consider the following normalized form of model parameters

$\tilde{\blacksquare} = \frac{\blacksquare}{\bar{\phi}_r}$, where ■, represents a model parameter, and the normalized model parameters are denoted as $\tilde{a}_1$, $\tilde{b}_1$, and $\tilde{b}_2$. In the present case, the axial displacement, $\bar{\tilde{\phi}}_1$, transverse displacement, $\bar{\tilde{\phi}}_2$, and rotation, $\tilde{\psi}_{21}$, are related to their dimensionless counterparts through the following relationships

$$\begin{aligned}
\frac{\bar{\tilde{\phi}}_1}{\bar{\phi}_r} &= \tilde{a}_1\tilde{x} + \left(1-\tilde{a}_1\right)\tilde{x}^2, \\
\frac{\bar{\tilde{\phi}}_2}{\bar{\phi}_r} &= \tilde{b}_1\tilde{x} + \tilde{b}_2\tilde{x}^2 - \left(\tilde{b}_1+\tilde{b}_2\right)\tilde{x}^3, \\
\frac{\tilde{\psi}_{21}}{\bar{\phi}_r} &= 3\left(\tilde{b}_1+\tilde{b}_2\right)\left(\frac{1}{4} - \left(\tilde{x}-\frac{1}{2}\right)^2\right).
\end{aligned} \tag{44}$$

Two cases were considered. First, the focus was put on the deformation of granular bars with prescribed axial strain of ~0.035. Second, the full deformation (axial strain of 0.095) was considered. Measurements from two sets of samples were used as first step of parameter calibration, while the data from the third set was employed to assess model repeatability described later. Figure 5 shows the calibrated normalized parameters $\tilde{a}_1$, $\tilde{b}_1$, and $\tilde{b}_2$ for all granular bars for axial strains of 0.035 (two left columns) and 0.095 (two right columns), respectively. Further, Fig. 6 shows the goodness of the fits for the considered granular bar for axial strains of 0.035 (two top rows) and 0.095 (two bottom rows), respectively. The goodness of fit is shown with the symbol χ and is plotted separately for the predicted axial and transverse displacements, rotations, and the global response of the model. The goodness of fit for different fields is calculated as the RMS residual divided by the corresponding standard uncertainty, where the residuals are defined as the dimensionless differences between model prediction and experimental observation. The global goodness of fit, χ_{global}, is computed as the RMS of the goodness of fit in axial, transverse, and rotation components, and is an indicator of global quality of the model.

From the results reported in Figs. 5 and 6, the following comments can be made. Figure 5 shows that, for all the configurations of the grain-pair interaction, and for both considered axial strains, the parameter $\tilde{a}_1$ is never exactly unity, although its deviation from unity is typically small. This result implies a small contribution of the quadratic term to the nonlinearity of axial displacements. Further, the value of $\tilde{a}_1$ for each configuration is almost constant for both axial strain levels, and therefore is independent of the prescribed axial strain. Given the scatter observed in the plots corresponding to $\tilde{a}_1$ for all *b* and *t* values, an

average value of $\tilde{a}_1 = 0.982$ is reported to describe all the samples at all axial strains. Notably, based on model predictions, the quadratic term with coefficient $\tilde{a}_2 = 1 - \tilde{a}_1$ in the axial displacement emerges *only if* normal-rotational and shear-rotational stiffnesses are present. Therefore, it is reasonable to state that such mechanisms exist in the studied chiral granular bar. However, their corresponding stiffness values are likely to be small. Moreover, having similar $\tilde{a}_1$ values for all the samples allows us to conclude that the change in the geometrical parameters *t* and *b* has minimal influence on the axial behavior of the sample under tension predicted by the model. This statement is supported by considering the goodness of fits for the axial displacements where all χ_{axial} values are within a narrow range, and therefore suggests that all fits are of the same quality for each considered axial strain. However, the average value of χ_{axial} for an axial strain of 0.095 is almost two times larger than its counterpart for an axial strain of 0.035, which suggests a degradation in the quality of the model at larger strains to predict the axial behavior of the system.

Regarding the parameters $\tilde{b}_1$ and $\tilde{b}_2$, a large scatter is observed for the samples with $t = 0.3$ mm and $t = 0.6$ mm (Fig. 5) due to extremely soft grain-pair interaction mechanisms with very thin beams. For all the other specimens, only small fluctuations are observed for $\tilde{b}_1$ and $\tilde{b}_2$ with respect to the geometrical parameters *t* and *b* for an axial strain of 0.035, and average values of $\tilde{b}_1 = -0.902$ and $\tilde{b}_2 = 2.338$ are obtained for all the samples for this strain level. It is also noteworthy that the goodness-of-fits, $\chi_{\text{transverse}}$ and $\chi_{\text{rotational}}$, for an axial strain of 0.035 also show uniformity with little scatter for all specimens with varying *b* and *t* (except for the two samples with $t = 0.3$ mm and $t = 0.6$ mm) . Further, comparing $\chi_{\text{transverse}}$ and $\chi_{\text{rotational}}$ for the two groups of varying *b* and *t* for an axial strain of 0.035, the samples in the group of varying *b* are better described using the proposed model. Analyzing the results for different axial strain-levels, a decrease in magnitude is observed for $\tilde{b}_1$ and $\tilde{b}_2$, with average values $\tilde{b}_1 = -0.647$ and $\tilde{b}_2 = 1.813$ for an axial strain equal to 0.095. It is also notable that $\chi_{\text{transverse}}$ and $\chi_{\text{rotational}}$ values have increased for an axial strain 0.095 compared 0.035, which indicates a degradation in the quality of the model in predicting transverse displacements and rotations of grains at larger strains. The change observed in $\tilde{b}_1$ and $\tilde{b}_2$ for higher strains is indicative of the evolution in grain-pair stiffnesses as the deformation progresses. Such progressive degradation of stiffnesses is potentially due to a significant influence of nonlinearities (both geometrical and material) in the grain-pair interaction mechanisms. It is also observed that for both axial

strains and, for nearly all samples, the quality of transverse displacement predictions is better than that of grain rotation predictions.

In general, and for both axial strains, $\chi_{\text{transverse}}$ and $\chi_{\text{rotational}}$ assume larger values than χ_{axial}. This effect is partly due to the fact that the model predicts coupled transverse displacement and rotation (and hence are more constrained) than the uncoupled axial displacement. It is also observed that all χ values increase as the deformation progresses. The model predictions are less correct at larger strains. This trend is presumably caused by nonlinearities in the grain-pair interaction, which become increasingly significant as loading progresses, while the model is predicated upon linear interaction mechanisms between grains. Moreover, an increase in $\chi_{\text{transverse}}$ and $\chi_{\text{rotational}}$ values is observed as the geometrical parameter *t* increases for an axial strain of 0.095. This increase suggests that the model is less predictive in granular systems with larger geometrical parameter *t* in the large strain regime.

The repeatability of both experimental and theoretical results is further investigated in the small deformation range (axial strain equal to 0.035) through tensile tests performed, as mentioned before, on a third set of 14 samples, such that there are altogether three independent repeats for each specimen type. Figures 7 and 8 give updates to the calibrated parameters and the goodness of fit using the results of these additional experiments. It is notable that the general trends with respect to the parameters $\tilde{a}_1$, $\tilde{b}_1$ and $\tilde{b}_2$ remain unchanged, although there is some increase in the spread, which nevertheless remains within ca. ±5% of the average value. Notably, the goodness of fit remains virtually unchanged (Fig. 8). In Fig. 9, direct comparisons of the calibrated and measured data are shown for selected cases. The agreement between the measured data and model predictions is excellent for the axial deformation. Further, it is seen that the model replicates very well the trends of the transverse deformations and rotations, both qualitatively and quantitatively, although with some scatter. It is also noteworthy that both transverse deformations and rotations are generally one order of magnitude lower than axial deformations, thus more sensitive to small imperfections in the fabrication process as well as measurement uncertainties. Last, it is observed that for the same prescribed axial deformation, the transverse deformations and rotations depend upon the geometrical parameters of the interconnections. In the examples given in Fig. 9, it is noteworthy that the maximum transverse deformations and rotations are larger for higher *t*. At the normalized axial displacement, $\tilde{\tilde{\phi}}_1$ =0.035, for the case of *t* = 0.7mm (Fig. 9a-c), the normalized transverse displacement, $\tilde{\tilde{\phi}}_2$ ranges from ca. $-3\text{x}10^{-3}$ to $1\text{x}10^{-3}$, and the maximum normalized rotation, $\tilde{\psi}_{21}$, is ca. 0.035. On the other hand, tt approximately the same normalized axial displacement for the case of *t* = 1.8mm (Fig. 9g-i), the

normalized transverse displacement, $\tilde{\tilde{\phi}}_2$ ranges from ca. -3x10^{-3} to 3x10^{-3}, and the maximum normalized rotation, $\tilde{\psi}_{21}$, is ca. 0.045.

3.3.2. Variation in deformation mechanism

Finally, it is useful to highlight a transition of deformation mechanisms within the range of considered geometrical parameters *b* and *t*, and further expatiate the emergence of nonlinearities in grain-pair interactions. Figures 10 and 11 show the dimensionless strain energy density distribution for geometries for axial strains equal to 0.035 and 0.095, respectively. While the strain energy density magnitude is different in granular bars between the two axial strains (as expected), a similar deformation mechanism is observed for each granular bar for both axial strains. It is notable that as the geometrical parameter *b* increases, the main deformation mechanism shifts from the two beams identified with *b* to the middle beam identified with *t*. Conversely, for small values of the geometrical parameter *t*, the middle beam identified with *t* undergoes maximum deformation, and as *t* increases, the deformation of the two beams identified with their thickness *b* becomes dominant. These variations in strain energy distributions within the grain-pair interactions are connected to the emergent transverse displacements and rotations at the mesoscale. For example, grain transverse displacement and rotations for specimen *b* = 0.8 mm and *t* = 0.7 mm are smaller than those for specimen *b* = 1.0 mm and *t* = 1.8 mm (Fig. 9). It is seen that in the first case the strain energy is distributed among all the three elements of grain-pair interaction (shown in the first row of Fig. 10), while for the second case, the strain energy is concentrated in the two vertical elements of grain-pair interaction (second row of Fig. 10). The emergent non-standard behavior predicted by the derived 1D micropolar model can be modulated by grain-pair interaction by making small variations in the inter-connection geometries.

Further, it is worth noting that the observed trends of $\chi_{\text{transverse}}$ and $\chi_{\text{rotational}}$ for an axial strain of 0.095 (Fig. 6) can be explained using Fig. 11. In particular, for samples with very small *b*, it is the geometric nonlinearity, and for samples with very large *b*, the material nonlinearity that are the main causes for lower model quality (i.e., larger $\chi_{\text{transverse}}$ and $\chi_{\text{rotational}}$ values). This effect contributes to having large $\chi_{\text{transverse}}$ and $\chi_{\text{rotational}}$ values in both ends of the spectrum and lower values for samples in the middle of the range. For samples with very small *t*, it is dominated by material nonlinearity, while for samples with very large *t*, the geometrical nonlinearity is the primary reason for lower model quality (i.e., larger $\chi_{\text{transverse}}$ and $\chi_{\text{rotational}}$ values) for large axial strains. In particular, the model quality decreases considerably as the geometrical parameter *t* increases for an axial strain of 0.095, and, in this case, the geometrical nonlinearity has a more pronounced effect on the predictive capability of the model.

4. SUMMARY AND CONCLUSION

The key findings of the presented work relate to the emergent chiral behavior of bars under extension such that the axis of chirality is orthogonal to the beam axis. The obtained results from both experimental and theoretical efforts show that this type of chirality arises in a granular motif through stretch-shear-rotation coupling of grain-pair interactions. The paper has presented a micropolar model based on a granular micromechanics approach (GMA) to describe the chiral behavior of 1D granular strings. The proposed model incorporates normal, shear, and rotational stiffnesses, along with normal-shear, normal-rotational, and shear-rotational coupling stiffnesses, all modeled as linear deformation mechanisms. The model predicts the behavior of chiral granular bars subjected to uniaxial tension, particularly non-standard transverse and rotational motions.

Inspired by this theoretical model, chiral granular bars with particular interaction mechanisms were designed, fabricated using 3D printing, and tested in a uniaxial testing machine. Digital image correlation (DIC) was carried out to measure full-field deformations of the tested specimens. Results obtained from DIC affirm that the designed constructs are representative of granular media composed of rigid grains interacting with each other through grain-pair interaction mechanisms. Repeatability of the measurements was demonstrated via experiments performed on three independent replications for every specimen.

The range of validity of the derived micropolar model was assessed by calibration against experimentally measured displacements and rotation fields of the studied granular bars. It was found that the model correctly predicted non-standard transverse deformations and rotations under bar extension, and that the calculations closely matched the measured deformations at small strain levels. The close agreement shows that the complex phenomena that occur in interacting grain pairs was well represented in the linear model by incorporating couplings between *all* deformation mechanisms. However, at higher strain levels, in which both material and geometrical nonlinearities become significant, large transverse displacements and rotations were observed in the grains nearest the boundaries of the bars, although the deformation trends were essentially replicated. These departures from the calculated responses are likely due to the effect of boundary layer and nonlinear interactions between grains. The present linear model is therefore limited to describing the overall behavior of the system far from boundaries and for small axial strains.

The findings of this work suggest future enhancements in both the theoretical model and the experimental campaign. From a theoretical viewpoint, there is need to introduce additional kinematic features [39], which may allow for the prediction of boundary layers as well the evaluation of deformation under multiple

boundary conditions. These theoretical predictions would need corresponding experimental investigations in which the boundary conditions and the geometric features were controlled with greater precision, which may better reveal the effect of microfeatures at the macroscale.

Statement of Competing Interest

The authors have no competing interests to declare.

Acknowledgements

This research is supported in part by the United States National Science Foundation grant CMMI -1727433.

Appendix A: Determination of Model Parameters from Mesoscale DIC Analyses

To obtain the model parameters $a_i, e_i, i \in \{0, 1, 2\}, b_i, i \in \{0, 1, 2, 3\}$, a least squares optimization with equality constraints was adopted. Explicitly, the cost function $f(\breve{\mathbf{x}}) = \| \breve{\mathbf{A}}\breve{\mathbf{x}} - \breve{\mathbf{b}} \|^2$ was minimized subject to linear constraints $\breve{\mathbf{C}}\breve{\mathbf{x}} = \breve{\mathbf{d}}$, where, $\breve{\mathbf{x}}$ is a column vector of length 10 and is composed of the unknown model parameters $a_i, e_i, i \in \{0, 1, 2\}, b_i, i \in \{0, 1, 2, 3\}$, $\breve{\mathbf{A}}$ a 33-by-10 matrix with nonzero components with respect to the location of grains according to Eq. (28), and $\breve{\mathbf{b}}$ a column vector of length 33 with its components being the grain displacements and rotations based upon mesoscale DIC analyses. The matrix $\breve{\mathbf{C}}$ is 7-by-10 and together with the 7-vector $\breve{\mathbf{d}}$ provide the linear constraints

$$\begin{aligned}
&a_0 = \text{measured axial displacement of grain adjacent to fixed grip,}\\
&a_0 + a_1 + a_2 = \text{measured axial displacement of grain adjacent to moving grip,}\\
&b_0 = \text{measured transverse displacement of grain adjacent to fixed grip,}\\
&b_0 + b_1 + b_2 + b_3 = \text{measured transverse displacement of grain adjacent to moving grip,}\\
&e_0 = \text{measured rotation of grain adjacent to fixed grip,}\\
&e_0 + e_1 + e_2 = \text{measured rotation of grain adjacent to moving grip,}
\end{aligned} \tag{A1}$$

and the relationship $e_1 + 3b_3 = 0$. Introducing the Lagrange multiplier vector $\breve{\mathbf{z}}$, setting up the Lagrangian cost function, and requiring it to be mutually minimized, one needs to solve the following system of equations to obtain the sought parameters and Lagrange multipliers

$$\begin{bmatrix} \breve{\mathbf{A}}^T\breve{\mathbf{A}} & \breve{\mathbf{C}}^T \\ \breve{\mathbf{C}} & \mathbf{0} \end{bmatrix} \begin{bmatrix} \breve{\mathbf{x}} \\ \breve{\mathbf{z}} \end{bmatrix} = \begin{bmatrix} \breve{\mathbf{A}}^T\breve{\mathbf{b}} \\ \breve{\mathbf{d}} \end{bmatrix}. \tag{A2}$$

Moreover, each row of $\breve{\mathbf{A}}$ and $\breve{\mathbf{b}}$ corresponding to displacements was divided by the corresponding standard uncertainty, and each row of $\breve{\mathbf{A}}$ and $\breve{\mathbf{b}}$ corresponding to rotations was divided by the corresponding uncertainty. To improve the conditioning of the system of equations (44), $\breve{\mathbf{C}}$ and $\breve{\mathbf{d}}$ were multiplied by $\dfrac{\text{norm}\left(\breve{\mathbf{A}}\right)}{\text{norm}\left(\breve{\mathbf{C}}\right)}$.

Due to the linear constraints, the model parameters a_0, b_0, and e_0 assume negligible values, and the other model parameters follow relationships (32).

References

[1] Kelvin WTB. The molecular tactics of a crystal. Oxford, England: Clarendon Pres; 1894.

[2] Takane D, Wang Z, Souma S, Nakayama K, Nakamura T, Oinuma H, et al. Observation of Chiral Fermions with a Large Topological Charge and Associated Fermi-Arc Surface States in CoSi. Phys Rev Lett 2019;122. https://doi.org/10.1103/PhysRevLett.122.076402.

[3] Nguyen LA, He H, Pham-Huy C. Chiral drugs: an overview. Int J Biomed Sci 2006;2:85–100.

[4] Ni X, Weiner M, Alù A, Khanikaev AB. Observation of higher-order topological acoustic states protected by generalized chiral symmetry. Nat Mater 2019;18:113–20. https://doi.org/10.1038/s41563-018-0252-9.

[5] Nieves MJ, Carta G, Jones IS, Movchan AB, Movchan N V. Vibrations and elastic waves in chiral multi-structures. J Mech Phys Solids 2018;121:387–408. https://doi.org/10.1016/j.jmps.2018.07.020.

[6] Wu W, Hu W, Qian G, Liao H, Xu X, Berto F. Mechanical design and multifunctional applications of chiral mechanical metamaterials: A review. Mater Des 2019;180:107950. https://doi.org/10.1016/j.matdes.2019.107950.

[7] Spadoni A, Ruzzene M, Gonella S, Scarpa F. Phononic properties of hexagonal chiral lattices. Wave Motion 2009;46:435–50. https://doi.org/10.1016/j.wavemoti.2009.04.002.

[8] Rosi G, Auffray N. Anisotropic and dispersive wave propagation within strain-gradient framework. Wave Motion 2016;63:120–34. https://doi.org/10.1016/j.wavemoti.2016.01.009.

[9] Liu XN, Hu GK, Sun CT, Huang GL. Wave propagation characterization and design of two-dimensional elastic chiral metacomposite. J Sound Vib 2011;330:2536–53. https://doi.org/10.1016/j.jsv.2010.12.014.

[10] Chen Y, Frenzel T, Guenneau S, Kadic M, Wegener M. Mapping acoustical activity in 3D chiral mechanical metamaterials onto micropolar continuum elasticity. J Mech Phys Solids 2020;137:103877. https://doi.org/10.1016/j.jmps.2020.103877.

[11] Frenzel T, Köpfler J, Jung E, Kadic M, Wegener M. Ultrasound experiments on acoustical activity in chiral mechanical metamaterials. Nat Commun 2019;10:1–6. https://doi.org/10.1038/s41467-019-11366-8.

[12] Alderson A, Alderson KL, Attard D, Evans KE, Gatt R, Grima JN, et al. Elastic constants of 3-, 4- and 6-connected chiral and anti-chiral honeycombs subject to uniaxial in-plane loading. Compos Sci Technol 2010;70:1042–8. https://doi.org/10.1016/j.compscitech.2009.07.009.

[13] Dirrenberger J, Forest S, Jeulin D, Colin C. Homogenization of periodic auxetic materials. Procedia Eng., vol. 10, Elsevier Ltd; 2011, p. 1847–52. https://doi.org/10.1016/j.proeng.2011.04.307.

[14] Poncelet M, Somera A, Morel C, Jailin C, Auffray N. An experimental evidence of the failure of Cauchy elasticity for the overall modeling of a non-centro-symmetric lattice under static loading. Int J Solids Struct 2018;147:223–37. https://doi.org/10.1016/j.ijsolstr.2018.05.028.

[15] Frenzel T, Kadic M, Wegener M. Three-dimensional mechanical metamaterials with a twist. Science (80-) 2017;358:1072–4. https://doi.org/10.1126/science.aao4640.

[16] Biswas R, Poh LH, Shedbale AS. A micromorphic computational homogenization framework for auxetic tetra-chiral structures. J Mech Phys Solids 2020;135:103801.

https://doi.org/10.1016/j.jmps.2019.103801.

[17] Lakes R. Elastic and viscoelastic behavior of chiral materials. Int J Mech Sci 2001;43:1579–89. https://doi.org/10.1016/S0020-7403(00)00100-4.

[18] Kadic M, Diatta A, Frenzel T, Guenneau S, Wegener M. Static chiral Willis continuum mechanics for three-dimensional chiral mechanical metamaterials. Phys Rev B 2019;99:214101. https://doi.org/10.1103/PhysRevB.99.214101.

[19] Misra A, Nejadsadeghi N, De Angelo M, Placidi L. Chiral metamaterial predicted by granular micromechanics: verified with 1D example synthesized using additive manufacturing. Contin Mech Thermodyn 2020;32. https://doi.org/10.1007/s00161-020-00862-8.

[20] Ha CS, Plesha ME, Lakes RS. Chiral three-dimensional isotropic lattices with negative Poisson's ratio. Phys Status Solidi 2016;253:1243–51. https://doi.org/10.1002/pssb.201600055.

[21] Reasa DR, Lakes RS. Cosserat Effects in Achiral and Chiral Cubic Lattices. J Appl Mech 2019;86. https://doi.org/10.1115/1.4044047.

[22] Liu X, Hu G. Elastic metamaterials making use of chirality: A review. Stroj Vestnik/Journal Mech Eng 2016;62:403–18. https://doi.org/10.5545/sv-jme.2016.3799.

[23] Chen W, Huang X. Topological design of 3D chiral metamaterials based on couple-stress homogenization. J Mech Phys Solids 2019;131:372–86. https://doi.org/10.1016/j.jmps.2019.07.014.

[24] Liu XN, Huang GL, Hu GK. Chiral effect in plane isotropic micropolar elasticity and its application to chiral lattices. J Mech Phys Solids 2012;60:1907–21. https://doi.org/10.1016/j.jmps.2012.06.008.

[25] Chen Y, Liu XN, Hu GK, Sun QP, Zheng QS. Micropolar continuum modelling of bi-dimensional tetrachiral lattices. Proc R Soc A Math Phys Eng Sci 2014;470:20130734. https://doi.org/10.1098/rspa.2013.0734.

[26] Giorgio I, Dell'Isola F, Misra A. Chirality in 2D Cosserat media related to stretch-micro-rotation coupling with links to granular micromechanics. Int J Solids Struct 2020;202:28–38. https://doi.org/10.1016/j.ijsolstr.2020.06.005.

[27] Duan S, Wen W, Fang D. A predictive micropolar continuum model for a novel three-dimensional chiral lattice with size effect and tension-twist coupling behavior. J Mech Phys Solids 2018;121:23–46. https://doi.org/10.1016/j.jmps.2018.07.016.

[28] Jiang Y, Li Y. Novel 3D-Printed Hybrid Auxetic Mechanical Metamaterial with Chirality-Induced Sequential Cell Opening Mechanisms. Adv Eng Mater 2018;20:1700744. https://doi.org/10.1002/adem.201700744.

[29] Fernandez-Corbaton I, Rockstuhl C, Ziemke P, Gumbsch P, Albiez A, Schwaiger R, et al. New Twists of 3D Chiral Metamaterials. Adv Mater 2019;31:1807742. https://doi.org/10.1002/adma.201807742.

[30] Spadoni A, Ruzzene M. Elasto-static micropolar behavior of a chiral auxetic lattice. J Mech Phys Solids 2012;60:156–71. https://doi.org/10.1016/j.jmps.2011.09.012.

[31] Misra A, Placidi L, Dell'isola F, Barchiesi E. Identification of a geometrically nonlinear micromorphic continuum via granular micromechanics. Z Angew Math Phys 2021;72:157. https://doi.org/10.1007/s00033-021-01587-7.

[32] Nejadsadeghi N, Misra A. Extended granular micromechanics approach: a micromorphic theory of degree n. Math Mech Solids 2020;25:407–29. https://doi.org/10.1177/1081286519879479.

[33] Calladine CR, Drew H. Understanding DNA: the molecule and how it works. Academic Press; 1997.

[34] Healey TJ. Material symmetry and chirality in nonlinearly elastic rods. Math Mech Solids 2002;7:405–20. https://doi.org/10.1177/108128028482.

[35] Costello GA. Theory of wire rope. New York: Springer Science & Business Media; 1997.

[36] Mitov M. Cholesteric liquid crystals in living matter. Soft Matter 2017;13:4176–209. https://doi.org/10.1039/c7sm00384f.

[37] Nejadsadeghi N, Misra A. Role of higher-order inertia in modulating elastic wave dispersion in materials with granular microstructure. Int J Mech Sci 2020;185:105867. https://doi.org/10.1016/j.ijmecsci.2020.105867.

[38] Timofeev D, Barchiesi E, Misra A, Placidi L. Hemivariational continuum approach for granular solids with damage-induced anisotropy evolution. Math Mech Solids 2020;26:738–70. https://doi.org/10.1177/1081286520968149.

[39] Nejadsadeghi N, Misra A. On the statics and dynamics of granular-microstructured rods with higher order effects. Math Mech Solids 2021:108128652110099. https://doi.org/10.1177/10812865211009938.

[40] Poorsolhjouy P, Misra A. Granular micromechanics based continuum model for grain rotations and grain rotation waves. J Mech Phys Solids 2019;129. https://doi.org/10.1016/j.jmps.2019.05.012.

[41] Barchiesi E, dell'isola F, Bersani AM, Turco E. Equilibria determination of elastic articulated duoskelion beams in 2D via a Riks-type algorithm. Int J Non Linear Mech 2021;128:103628. https://doi.org/10.1016/j.ijnonlinmec.2020.103628.

[42] De Angelo M, Placidi L, Nejadsadeghi N, Misra A. Non-standard Timoshenko beam model for chiral metamaterial: Identification of stiffness parameters. Mech Res Commun 2020;103:103462. https://doi.org/10.1016/j.mechrescom.2019.103462.

[43] Eremeyev VA, Lebedev LP, Altenbach H. Foundations of micropolar mechanics. Springer Science & Business Media; 2012.

[44] Altenbach H, Eremeyev VA. On the linear theory of micropolar plates. ZAMM-Journal Appl Math Mech 2009;89:242–56.

[45] dell'Isola F, Barchiesi E, Misra A. Naïve Model Theory: its applications to the Theory of Metamaterials Design. In: Francesco dell'Isola, Steigmann D, editors. Discret. Contin. Model. Complex Mater., Cambridge, U.K.: Cambridge; 2020, p. 141–96. https://doi.org/10.1017/9781316104262.

[46] Leclerc H, Neggers J, Mathieu F, Roux S, Hild F. Correli 3.0. Agence pour la Protection des Programmes, Paris, 2015. IDDN FR n.d.;1.

[47] Sutton MA, Orteu JJ, Schreier H. Image correlation for shape, motion and deformation measurements: basic concepts, theory and applications. Springer Science & Business Media; 2009.

[48] Hild F, Roux S. Digital image correlation. In: Rastogi PK, Hack E, editors. Springer Ser. Mater. Sci., vol. 242, Weinheim, Germany: John Wiley & Sons; 2016, p. 57–129.

https://doi.org/10.1007/978-3-319-30954-5_3.

[49] Hild F, Misra A, dell'Isola F. Multiscale DIC Applied to Pantographic Structures. Exp Mech 2021;61:431–43. https://doi.org/10.1007/s11340-020-00636-y.

[50] Dell'Isola F, Seppecher P, Spagnuolo M, Barchiesi E, Hild F, Lekszycki T, et al. Advances in pantographic structures: design, manufacturing, models, experiments and image analyses. Contin Mech Thermodyn 2019. https://doi.org/10.1007/s00161-019-00806-x.

[51] Nejadsadeghi N, De Angelo M, Misra A, Hild F. Multiscalar DIC Analyses of Granular String Under Stretch Reveal Non-standard Deformation Mechanisms. Int J Solids Struct 2022; 239–240 (2022) 111402. https://doi.org/10.1016/j.ijsolstr.2021.111402

[52] Jones EM, Iadicola MA. A good practices guide for digital image correlation. Int Digit Image Correl Soc 2018;10. https://doi.org/10.32720/idics/gpg.ed1.

List of Figures

Fig 1 Prediction from the derived micropolar model of (a) axial displacement, (b) transverse displacement, and (c) rotation fields of a 1D chiral bar under uniaxial tension.

Fig 2. Proposed granular string with (a) its building-block geometry and specimen tested in the space of geometric parameters. (b) Image of speckle pattern on the surface of a specimen for digital image correlation (DIC) analyses. (c) Experimental and image acquisition setup.

Fig 3. Macro- and microscale DIC results for a granular string with t = 1.2 mm and b = 1 mm. (a) Initial, final and three intermediate images captured during the tensile test. (b) Finite element (FE) mesh for macroscale DIC. (c) FE mesh for microscale DIC. (d, f) Transverse and axial displacement fields, respectively, for the macroscale analysis. (e, g) Transverse and axial displacement fields, respectively, for the microscale analysis. (h) Root mean square (RMS) gray level residuals for the macroscale analyses. (i) RMS gray level residuals for the microscale analyses. (j-m) Transverse normal strain, axial normal strain, shear strain, and normalized strain energy for the microscale analysis.

Fig 4. Typical results from mesoscale DIC analyses shown for a granular string with t = 1.2 mm and b = 1 mm subjected to uniaxial extension. Each curve depicted by changing shade represents the end of a load increment as the experiment progresses. (a) Root mean square gray level residuals showing that DIC identification accuracy diminishes at larger loading. (b)-(d) Grain axial displacement, transverse displacement and rotation for different levels of overall axial extension.

Fig 5. Calibrated independent model parameters for applied axial strain 0.035 (two left columns) and 0.095 (two right columns) for varying geometric parameters b (a)-(c) and (g)-(i), and t (d)-(f) and (j)-(l). Deviation from unity of parameter $\tilde{a}_1$ (top row) indicates the contribution of the quadratic term to axial displacement. Parameters $\tilde{b}_1$ and $\tilde{b}_2$ (2nd and 3rd row) indicate complex dependence geometrical parameters b and t. Circles denote the mean values and crosses the extreme values.

Fig 6. Goodness of fit for applied axial strain 0.035 (two top rows or (a)-(h)) and 0.095 (two bottom rows or (i)-(p)) for varying geometrical parameters b (a)-(d) and (i)-(l), and t (e)-(h) and (m)-(p). Larger values at axial strain of 0.095 (row 3 and 4) indicates deteriorating fit with model compared to axial strain of 0.035 (row 1 and 2). Circles denote the mean values and crosses the extreme values.

Fig 7. Calibrated model parameters for an applied axial strain equal to 0.035 including data from additional experiments showing the repeatability of the results for (a) varying geometrical parameter b, and (b) for varying geometrical parameter t. Circles denote the mean values and crosses the extreme values.

Fig 8. Goodness of fit for an applied axial strain of 0.035 including data from additional experiments showing the repeatability of the results for (a)-(d) varying geometrical parameter b, and (e)-(h) for varying geometrical parameter t. Circles denote the mean values and crosses the extreme values.

Fig 9. Direct comparisons of predicted and measured grain axial displacement, transverse displacement and rotation for granular strings with (a)-(c) t = 0.7 mm and b = 0.8 mm, (d)-(f) t = 1.2 mm and b = 1 mm, and (g)-(i) t = 1.8 mm and b = 1 mm.

Fig 10. Strain energy density distribution in granular bar with different geometric parameters for applied axial strain 0.035. First row gives the results for varying geometrical parameter *b* of vertical elements in grain-pair interconnections and constant *t*=0.7mm of horizontal element. Second row gives the results for constant *b*=1.0 mm varying *t*.

Fig 11. Strain energy density distribution in granular bar with different geometric parameters for applied axial strain 0.095. First row gives the results for varying geometrical parameter *b* of vertical elements in grain-pair interconnections and constant *t*=0.7mm of horizontal element. Second row gives the results for constant *b*=1.0 mm varying *t*.

Table 1. DIC hardware parameters.

Camera	NIKON D300
Definition	4288 × 2848 pixels (RGB image)
Gray levels amplitude	8 bits
Lens	AF-S VR Micro-Nikkor 105mm f / 2.8G ED
Aperture	f / 4.5
Field of view	111 × 74 mm^2
Image scale	60 μm / px (B&W images)
Stand-off distance	≈ 90 cm
Image acquisition rate	1/5 fps
Exposure time	20 ms
Patterning technique	Sprayed black paint
Pattern feature size	2.6 px

Table 2. Standard uncertainties for the DIC analyses at different levels.

	Axial direction	Transverse direction	Rotation
Macroscale	0.024 px (1.5 μm)	0.024 px (1.5 μm)	-
Microscale	0.024 px (1.5 μm)	0.024 px (1.5 μm)	-
Mesoscale	0.021 px (1.3 μm)	0.021 px (1.3 μm)	1.5×10^{-4}

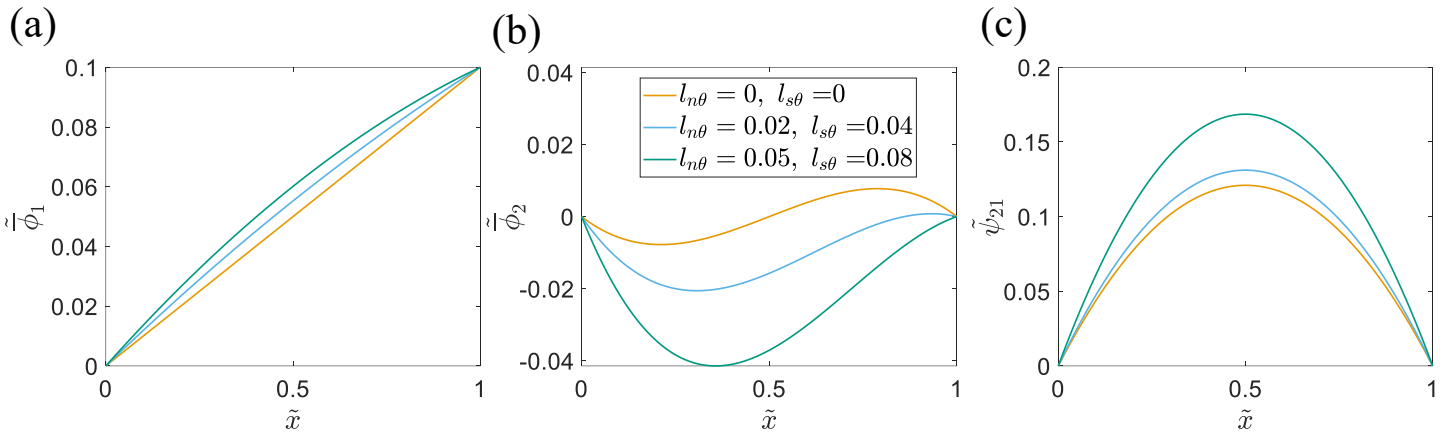

Fig 1. Prediction from the derived micropolar model of (a) axial displacement, (b) transverse displacement, and (c) rotation fields of a 1D chiral bar under uniaxial tension.

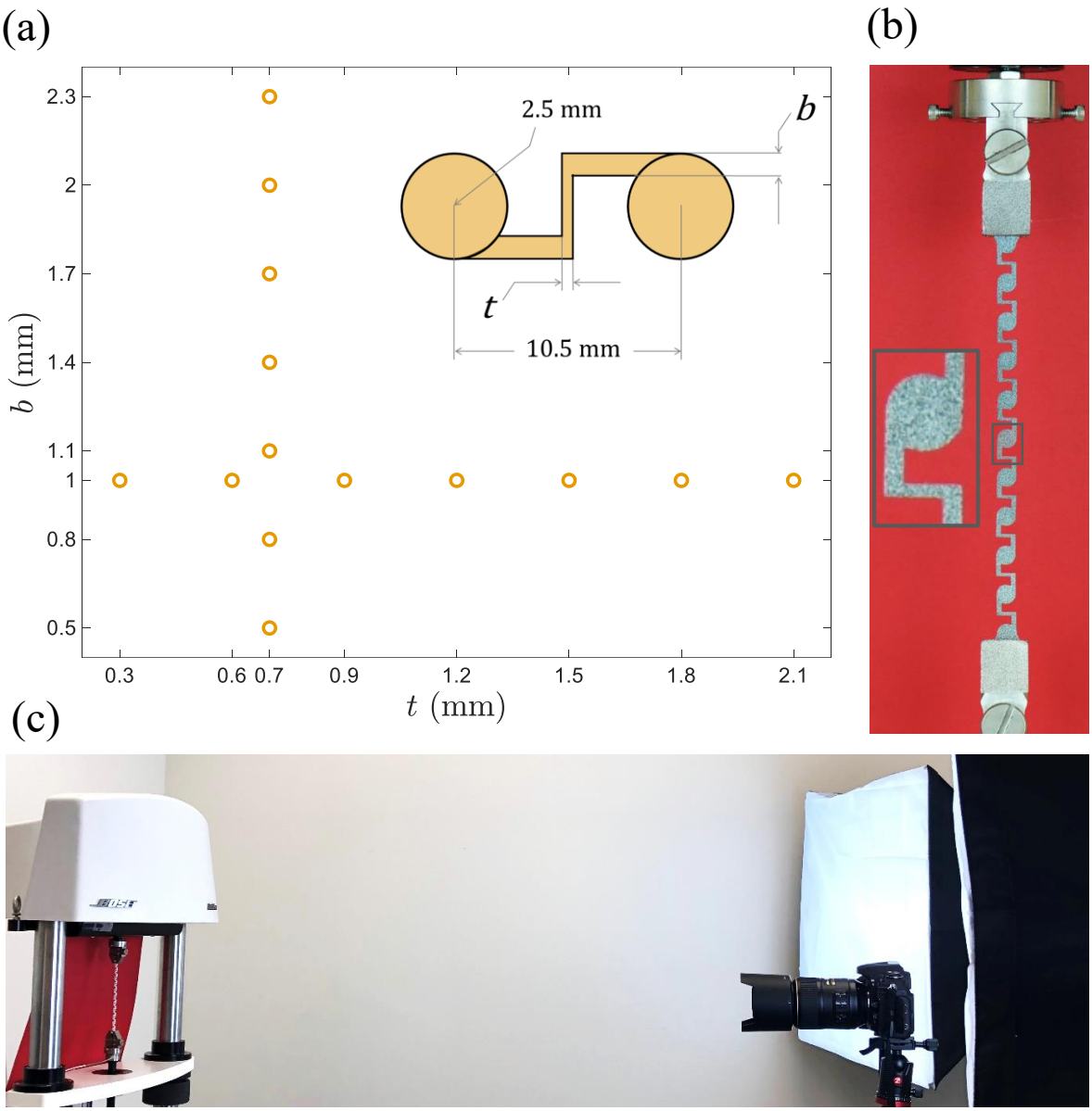

Fig 2. Proposed granular string with (a) its building-block geometry and specimen tested in the space of geometric parameters. (b) Image of speckle pattern on the surface of a specimen for digital image correlation (DIC) analyses. (c) Experimental and image acquisition setup.

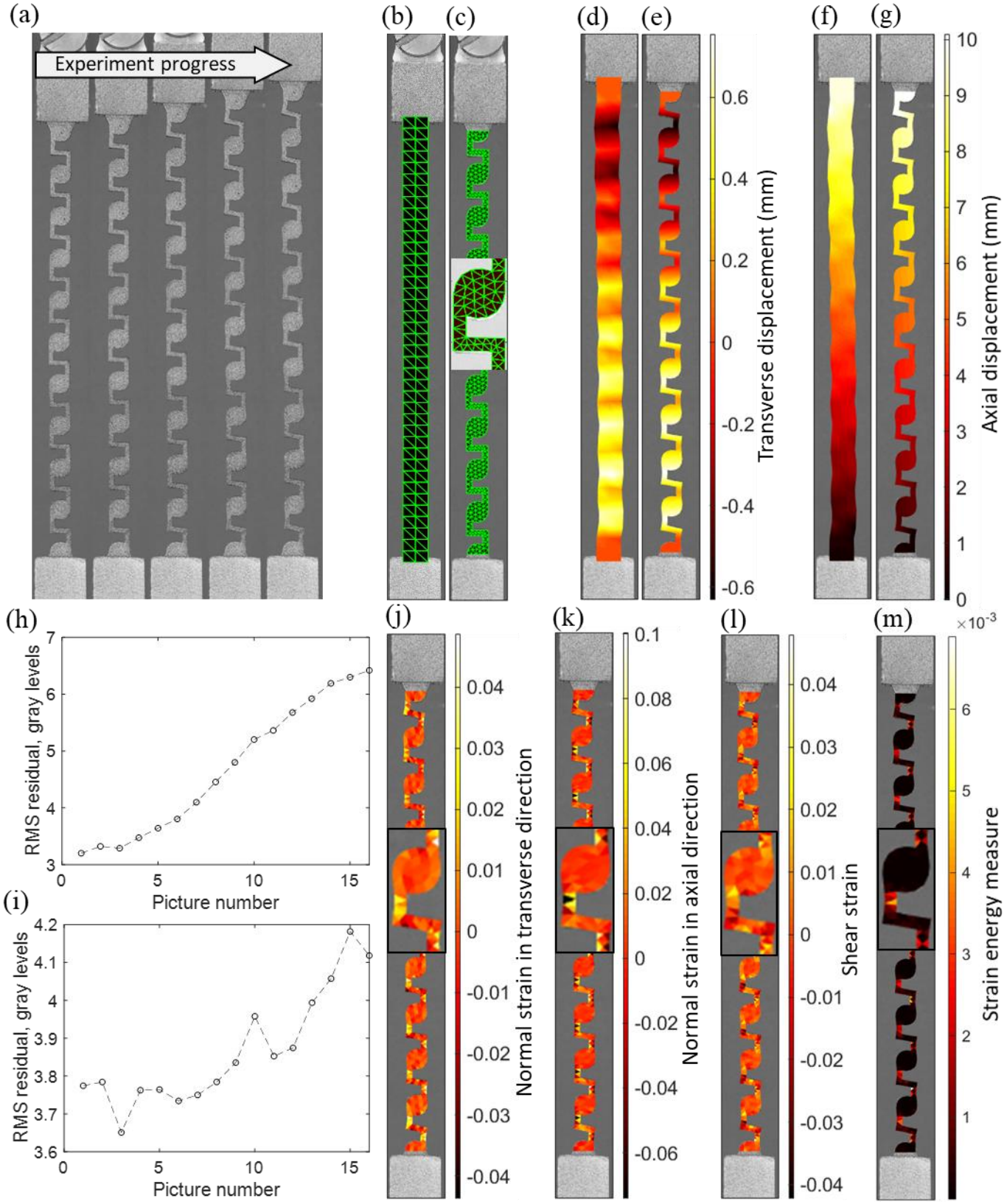

Fig 3. .Macro- and microscale DIC results for a granular string with t = 1.2 mm and b = 1 mm. (a) Initial, final and three intermediate images captured during the tensile test. (b) Finite element (FE) mesh for macroscale DIC. (c) FE mesh for microscale DIC. (d, f) Transverse and axial displacement fields, respectively, for the macroscale analysis. (e, g) Transverse and axial displacement fields, respectively, for the microscale analysis. (h) Root mean square (RMS) gray level residuals for the macroscale analyses. (i) RMS gray level residuals for the microscale analyses. (j-m) Transverse normal strain, axial normal strain, shear strain, and normalized strain energy for the microscale analysis.

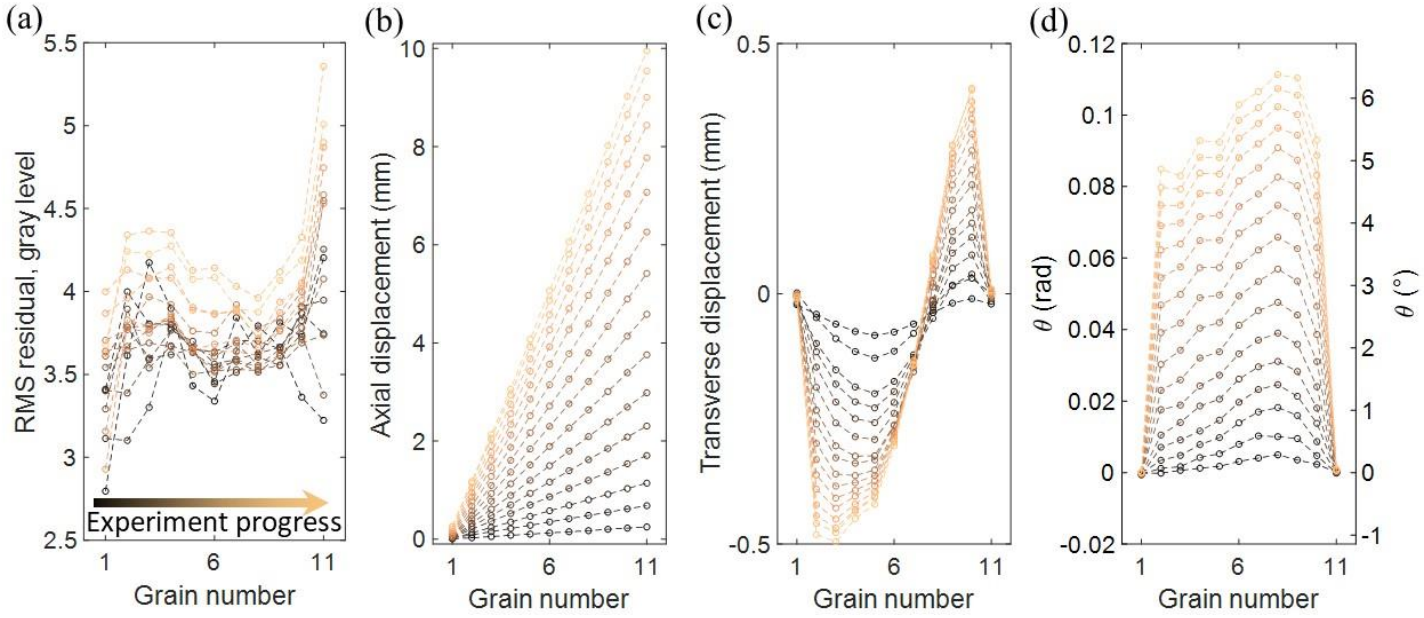

Fig 4. Typical results from mesoscale DIC analyses shown for a granular string with t = 1.2 mm and b = 1 mm subjected to uniaxial extension. Each curve depicted by changing shade represents the end of a load increment as the experiment progresses. (a) Root mean square gray level residuals showing that DIC identification accuracy diminishes at larger loading. (b)-(d) Grain axial displacement, transverse displacement and rotation for different levels of overall axial extension.

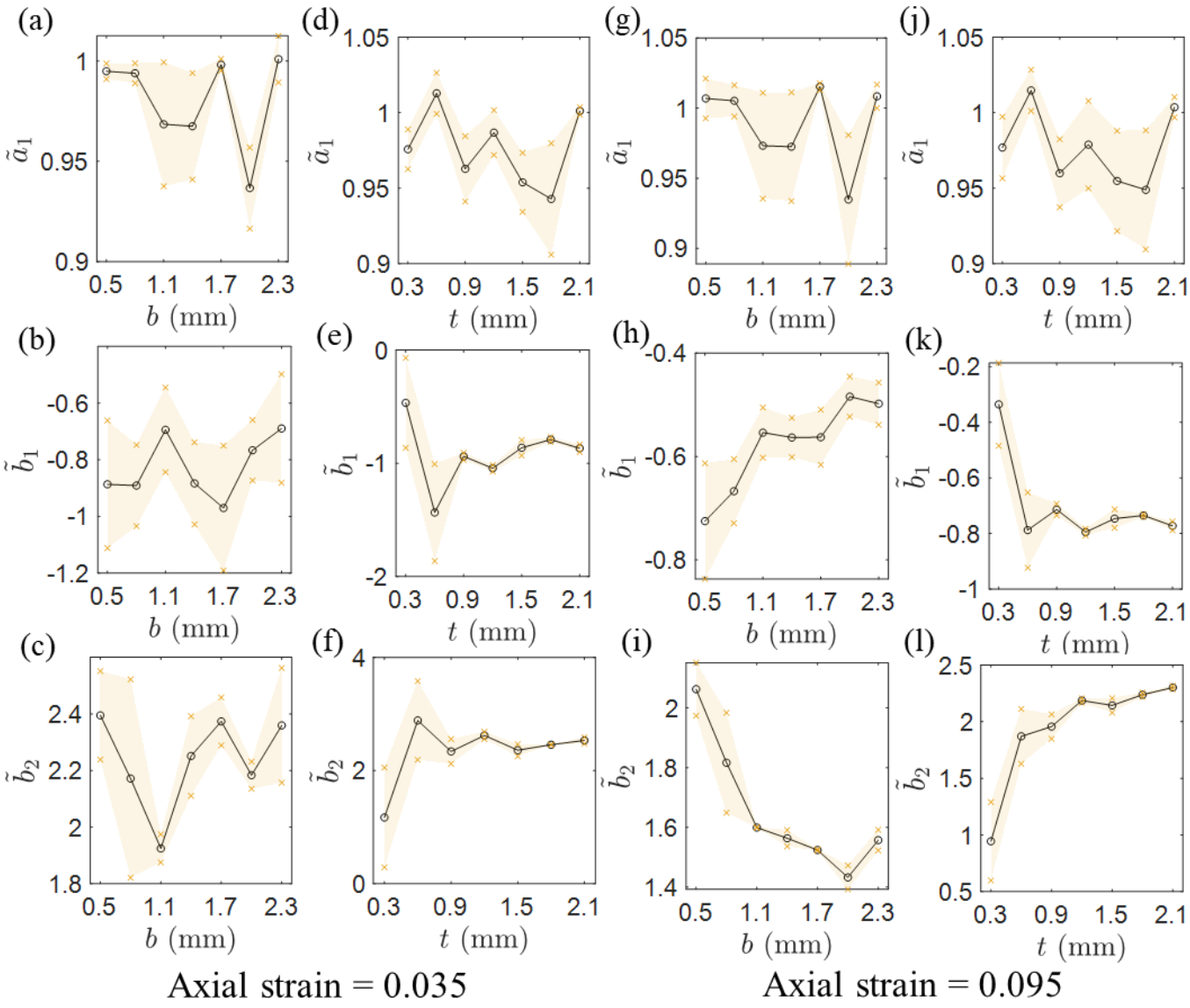

Fig 5. Calibrated independent model parameters for applied axial strain 0.035 (two left columns) and 0.095 (two right columns) for varying geometric parameters *b* (a)-(c) and (g)-(i), and *t* (d)-(f) and (j)-(l). Deviation from unity of parameter $\tilde{a}_1$ (top row) indicates the contribution of the quadratic term to axial displacement. Parameters $\tilde{b}_1$ and $\tilde{b}_2$ (2nd and 3rd row) indicate complex dependence geometrical parameters *b* and *t*. Circles denote the mean values and crosses the extreme values.

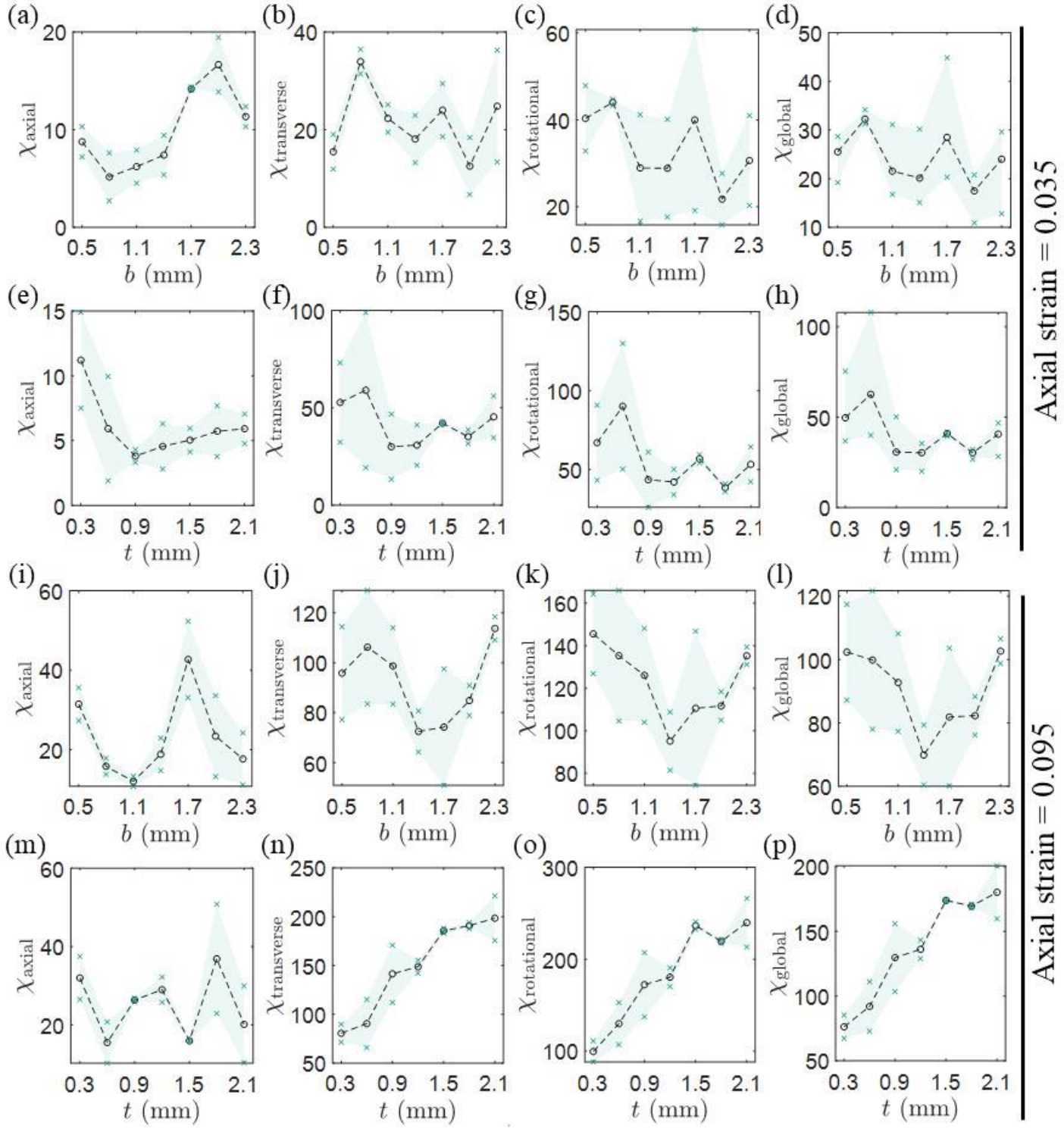

Fig 6. Goodness of fit for applied axial strain 0.035 (two top rows or (a)-(h)) and 0.095 (two bottom rows or (i)-(p)) for varying geometrical parameters *b* (a)-(d) and (i)-(l), and *t* (e)-(h) and (m)-(p). Larger values at axial strain of 0.095 (row 3 and 4) indicates deteriorating fit with model compared to axial strain of 0.035 (row 1 and 2). Circles denote the mean values and crosses the extreme values.

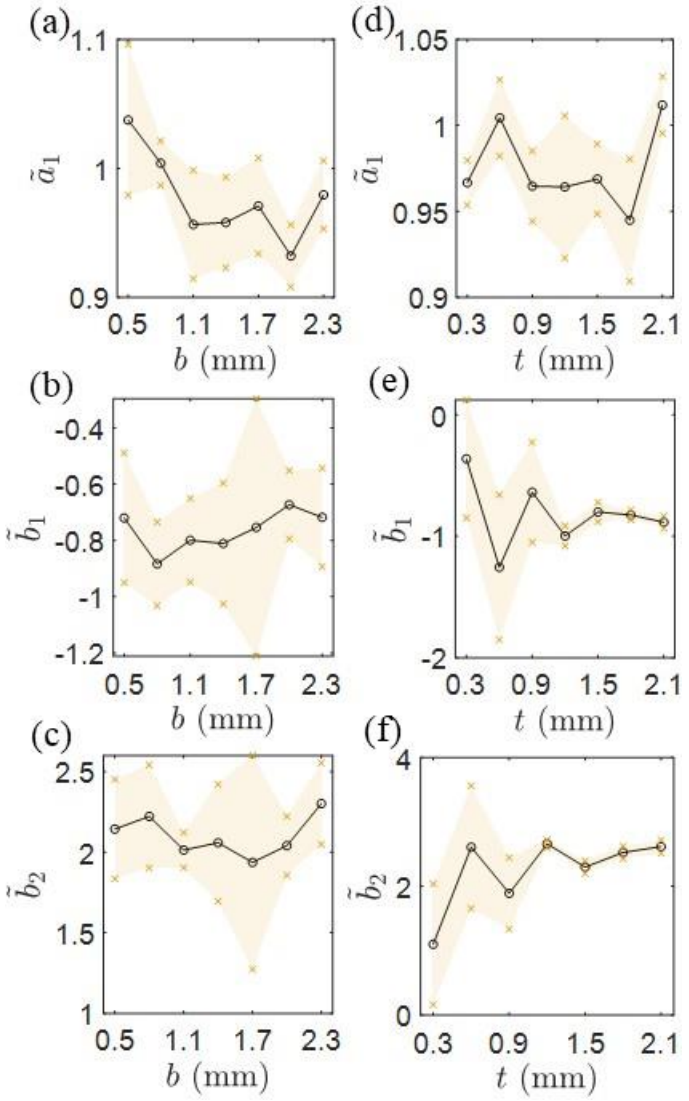

Fig 7. Calibrated model parameters for an applied axial strain equal to 0.035 including data from additional experiments showing the repeatability of the results for (a) varying geometrical parameter *b*, and (b) for varying geometrical parameter *t*. Circles denote the mean values and crosses the extreme values.

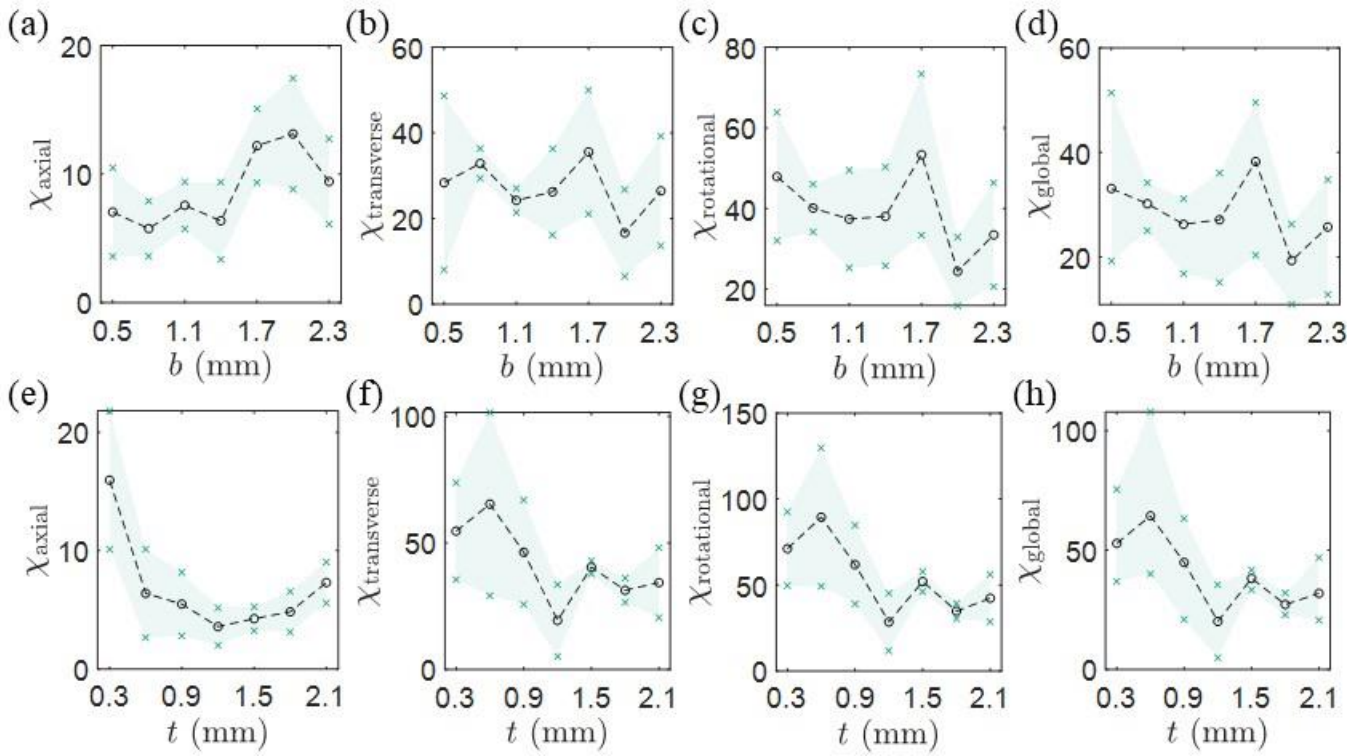

Fig 8. Goodness of fit for an applied axial strain of 0.035 including data from additional experiments showing the repeatability of the results for (a)-(d) varying geometrical parameter *b*, and (e)-(h) for varying geometrical parameter *t*. Circles denote the mean values and crosses the extreme values.

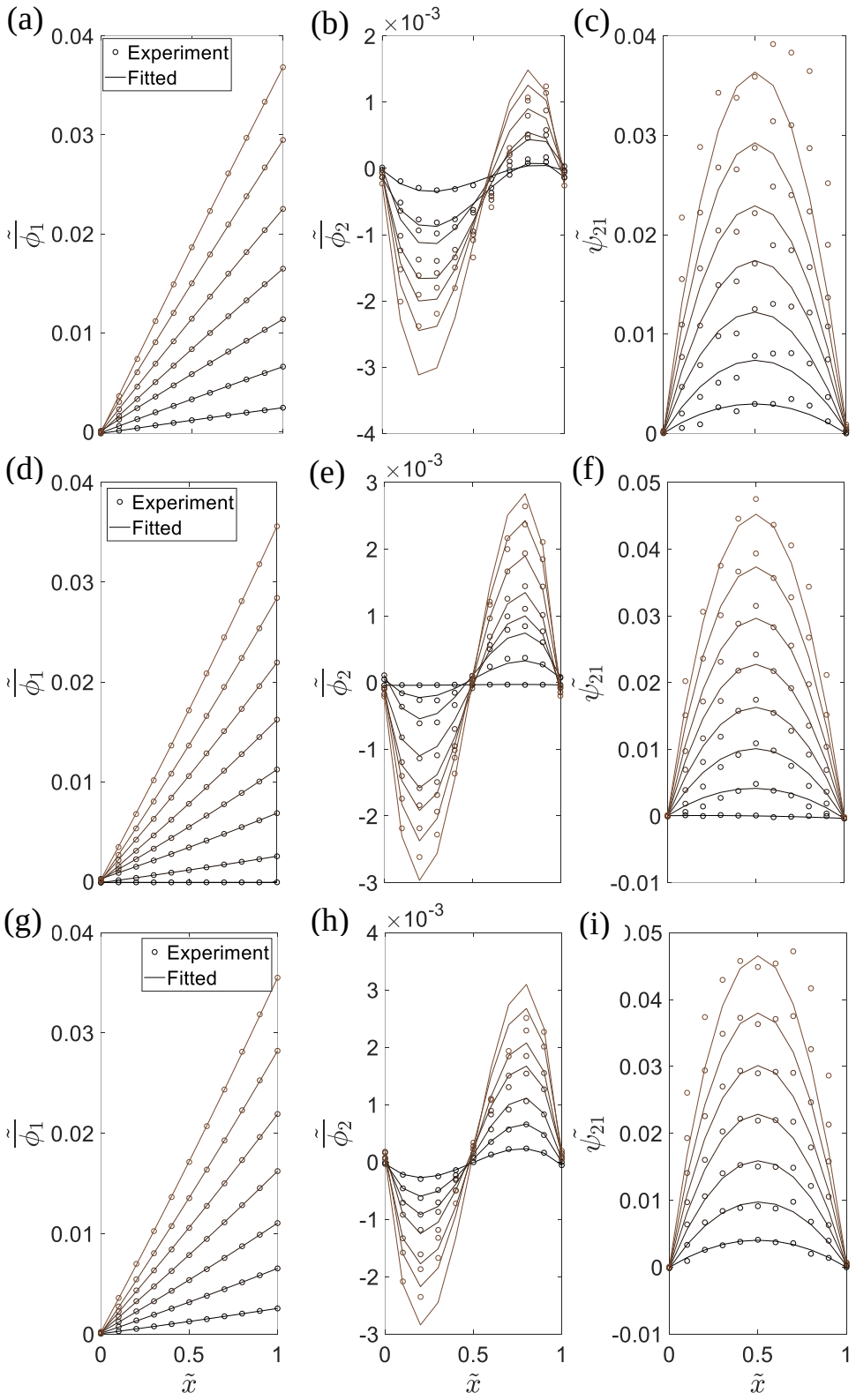

Fig 9. Direct comparisons of predicted and measured grain axial displacement, transverse displacement and rotation for granular strings with (a)-(c) t = 0.7 mm and b = 0.8 mm, (d)-(f) t = 1.2 mm and b = 1 mm, and (g)-(i) t = 1.8 mm and b = 1 mm.

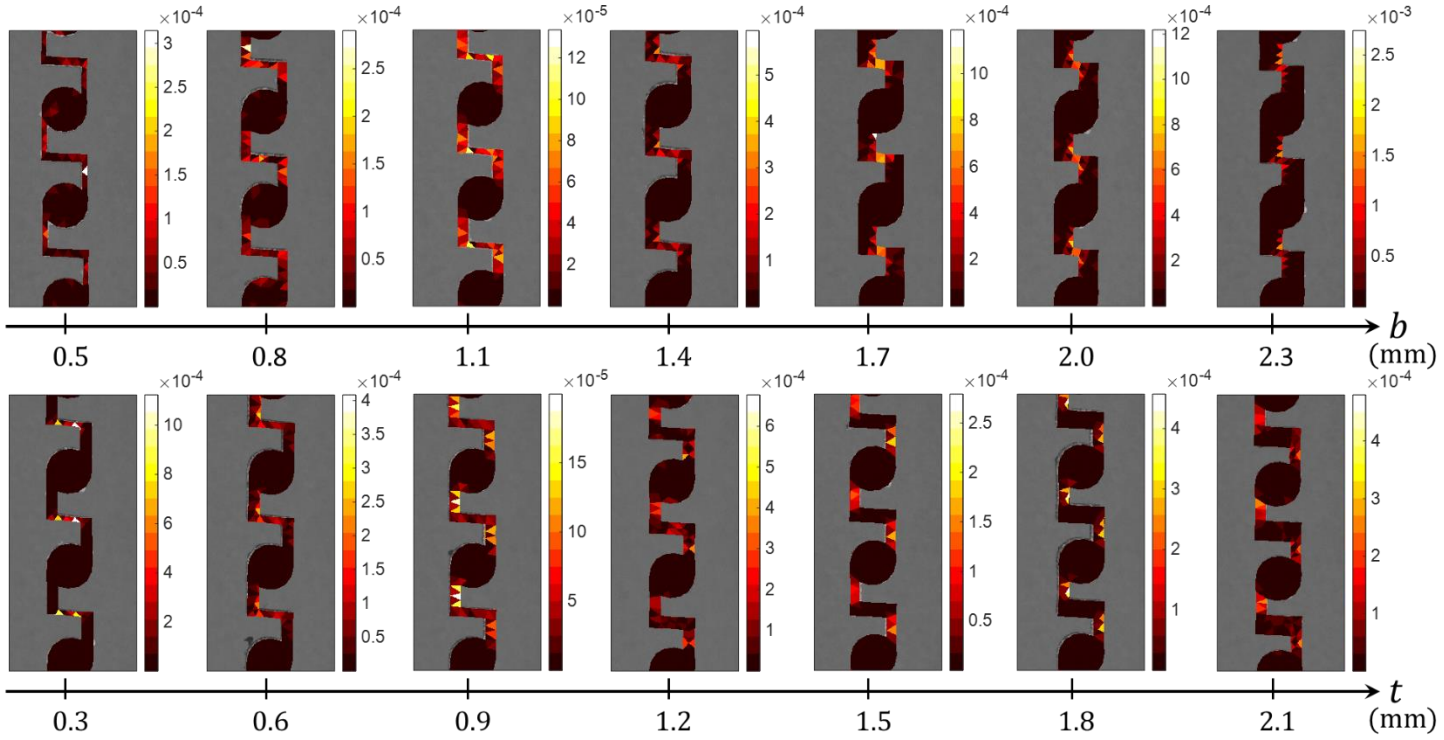

Fig 10. Strain energy density distribution in granular bar with different geometric parameters for applied axial strain 0.035. First row gives the results for varying geometrical parameter *b* of vertical elements in grain-pair interconnections and constant *t*=0.7mm of horizontal element. Second row gives the results for constant *b*=1.0 mm varying *t*.

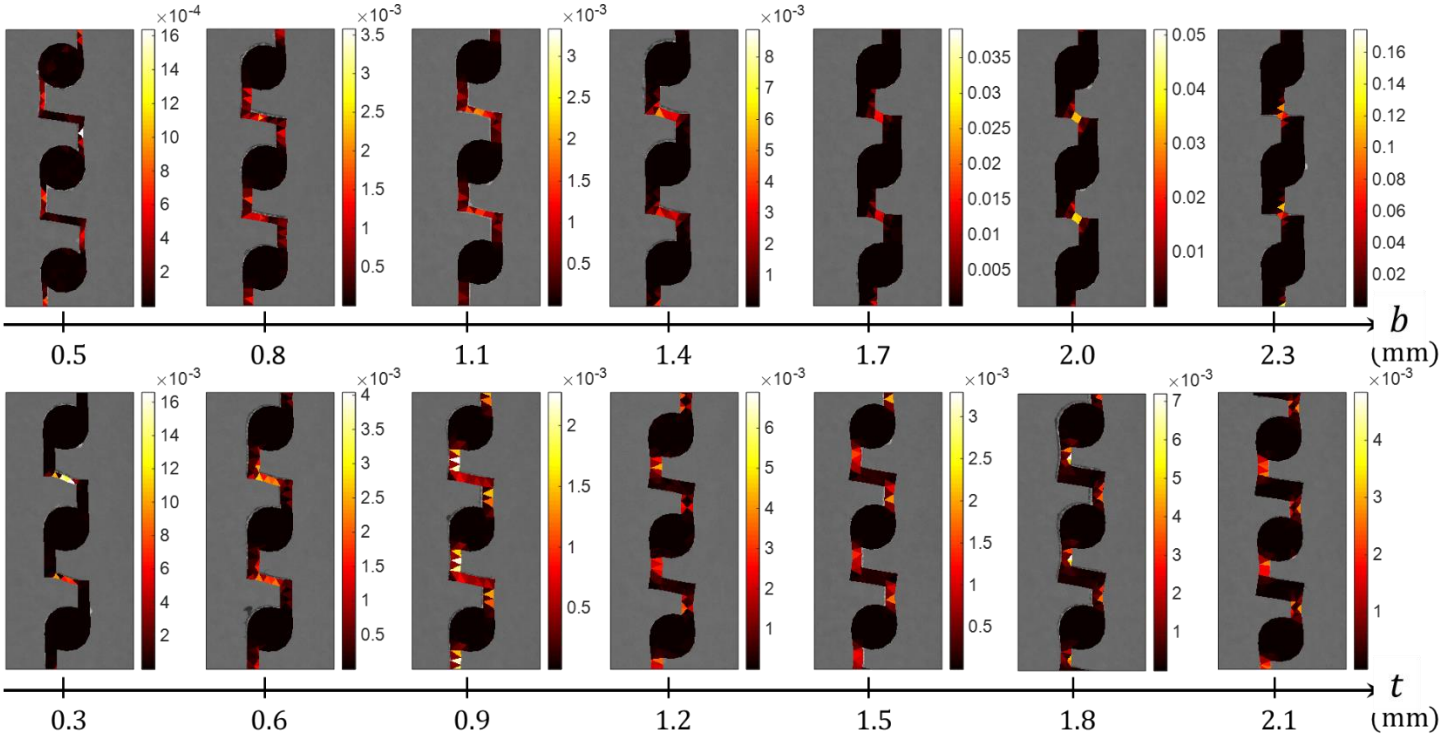

Fig 11. Strain energy density distribution in granular bar with different geometric parameters for applied axial strain 0.095. First row gives the results for varying geometrical parameter *b* of vertical elements in grain-pair interconnections and constant *t*=0.7mm of horizontal element. Second row gives the results for constant *b*=1.0 mm varying *t*.